THESIS FOR THE DEGREE OF LICENTIATE OF PHILOSOPHY

Methanol masers reveal the magnetic field of a high mass protostar

DARIA DALL'OLIO

Department of Space, Earth and Environment
CHALMERS UNIVERSITY OF TECHNOLOGY
Gothenburg, Sweden 2017

Methanol masers reveal the magnetic field of a high mass protostar
DARIA DALL'OLIO

Division of Astronomy & Plasma Physics
Department of Space, Earth and Environment
Chalmers University of Technology
SE–412 96 Gothenburg, Sweden
Phone: +46 (0)31–772 1000

Contact information:
Daria Dall'Olio
Onsala Space Observatory
Chalmers University of Technology
SE–439 92 Onsala, Sweden

Phone: +46 (0)31–772 5546
Fax: +46 (0)31–772 5590
Email: daria.dallolio@chalmers.se

Printed by Chalmers Reproservice
Chalmers University of Technology
Gothenburg, Sweden 2017

To Piero

Methanol masers reveal the magnetic field of a high mass protostar

DARIA DALL'OLIO
Department of Space, Earth and Environment
Chalmers University of Technology

Abstract

The role played by magnetic fields in high-mass star formation is not yet fully clear. Theoretical simulations have shown that magnetic fields appear to suppress fragmentation in the star forming cloud, to enhance accretion via disc and to provide feedback in the form of outflows and jets. However, models require specific magnetic configurations and need more observational constraints to properly test the impact of magnetic fields. The identification of massive protostars is complicated due to their quick evolution, and their location inside distant, dense, and dark clusters.

In the past few years, masers have been successfully used to probe the magnetic field strength and morphology at the small scales of about 10 astronomical units (au), around massive protostars. Thanks to the narrow and strong spectral lines of masers, we can measure linear polarization angles and Zeeman splitting and obtain information about the magnetic field intensity and geometry. Radio-interferometers, such as the Multi-Element Radio Linked Interferometer Network (MERLIN), can provide the sensitivity and the spatial and spectral resolution needed to detect the signatures of protostellar processes at the required scale of few au.

In this work we make use of MERLIN data to investigate the magnetic field structure of the massive protostar IRAS 18089-1722, analyzing 6.7 GHz methanol maser observations. IRAS 18089-1732 is a well studied high mass protostar, showing a hot core chemistry, an accretion disc and a bipolar outflow. An ordered magnetic field oriented around its disc has been detected from previous observations of polarized dust. This gives us the chance to investigate how the magnetic field at the small scale probed by masers relates to the large scale field probed by the dust.

Our analysis of the 6.7 GHz polarized methanol maser observations, indicates that the magnetic field in the maser region is consistent with the magnetic field constrained by the previous dust polarized observations. We find that the magnetic field in the maser region presents the same orientation as in the disc. Thus the large scale field component, even at the few au scale of the masers, dominates over any small scale field fluctuations. We present a tentative detection of circularly polarized line emission, from which we obtain a field strength along the line of sight of 5.5 mG, consistent with previous estimates.

Keywords: magnetic field – stars: formation – stars: massive – masers – polarization – stars: individual: IRAS 18089-1732

Research contributions

This thesis is based on the work contained in the following paper:

- D. Dall'Olio, W. H. T. Wlemmings, G. Surcis, H. Beuther, B. Lankhaar, M. V. Persson, A. M. S. Richards, E. Varenius:
  Methanol masers reveal the magnetic field of the high mass protostar IRAS 18089-1732
  submitted for publication in Astronomy & Astrophysics, (2017)

Other publications not included in this thesis

I also contributed to popular science publications and some of my works are:

- D. Dall'Olio:
  L'occhio di SKA e l'astronomia del futuro
  Popular science paper on the SKA telescope, published in Oculus Enoch – bulletin of the Planetarium of Ravenna, Apr. 2017;

- EVN Radionet3 QueSera group:
  Eagle View Network
  Popular science comic on the EVN history, published as result of EVN Radionet3 QueSera group activities, Oct. 2015;

- D. Dall'Olio:
  Costellazione Manga: le stelle nel fumetto e nel cinema di animazione giapponese
  Popular science article on Japanese comics and astronomy, published in Giornale di Astronomia, vol.41, no.1, Fabrizio Serra Editore, Mar. 2015.

Contents

Chapter 1

Introduction

The study of the formation and early evolution of stars is an active part of astrophysical research. The field involves complex physical and chemical processes not yet completely understood, and it brings up several open questions that need further insight.

A star is mostly made up of hydrogen and helium; heavier elements are present for a few per cent of the total mass and they are the outcome of nuclear fusion that occurred in stars of previous generations (Fig. 1.1). The star formation phase is the moment when the stellar mass is determined. The stellar mass and metallicity are important parameters, because they control the path of stellar evolution. Massive stars, for example, can explode as Type II Supernovae (SN), enriching the surrounding medium of new material and driving the structure and the chemistry evolution of the host galaxy. The strong ionizing ultra-violet (UV) radiation and the consequent formation of HII regions, along with stellar winds, and eventually Supernovae shocks, reshape and heat the interstellar medium (ISM). These phenomena can potentially trigger the formation of new stars, or destroy the clouds of gas suppressing the star formation process. Also low-mass stars undergo various stages of mass loss, for example during the giant phase or the planetary nebula stage. Moreover, stellar nurseries are also the places where complex organic molecules (COMs; they are considered the seeds of life) and planets are created. Therefore, answering the questions about stellar birth can shed some light on our own origins.

A wide range of problems needs to be investigated, and just a few examples of outstanding questions waiting for solutions are: Under which conditions does a cloud fragment and form associations of stars or clusters? Do low-mass and high-mass stars form by similar processes? What are the fundamental processes that regulate the evolution of outflows and jets? What is the mechanism that governs the discs? Which is the role played by magneto-hydrodynamics (MHD) in star formation?

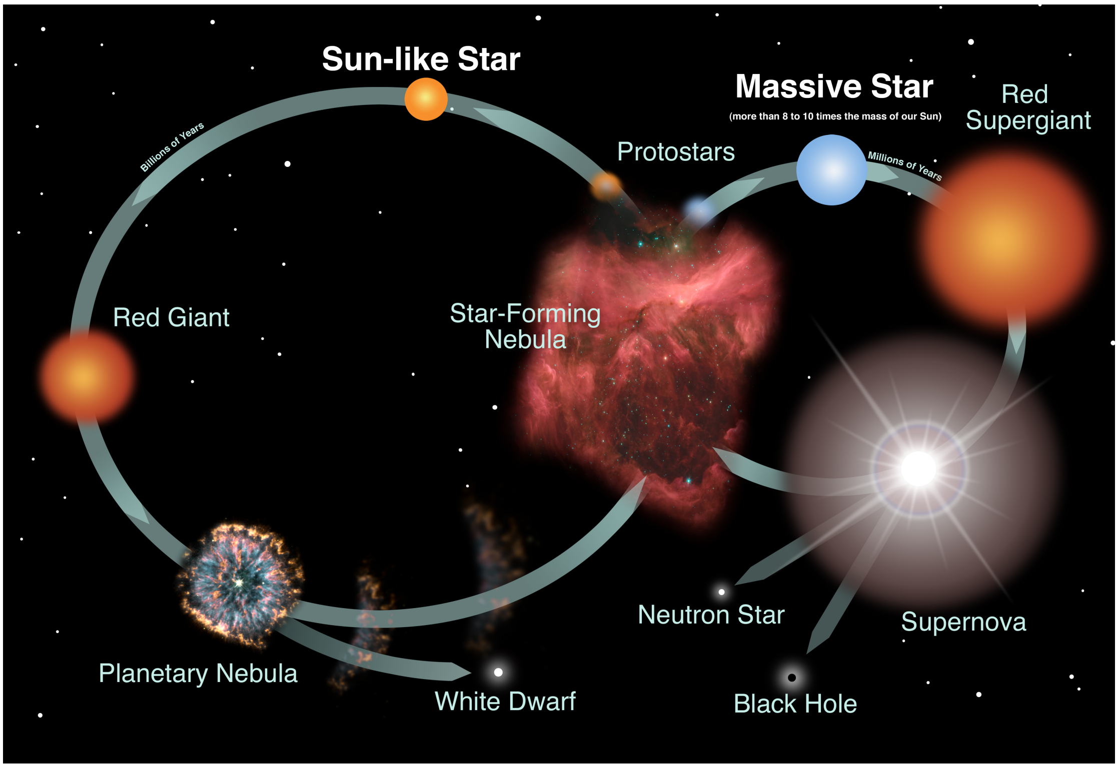

Figure 1.1: Illustration showing the life-cycle of Sun-like and massive stars. Star forming regions are the place where new stars are generated. At the end of their evolution the stars return enriched material to the interstellar medium; a new generation of stars can form from the debris of the previous one. (Credit: NASA and the Night Sky Network).

This thesis will focus on observing the role played by magnetic fields during the first phases of the high mass SF. The dramatic changes that occur in the deeply magnetized ISM and that lead to the dissipation of the magnetic field in a newborn star are still unclear. Consequently, the link between the magnetic field and the physical structure and dynamics of a pre-stellar embryo is also unknown. In order to investigate these processes, we need to peek inside the stellar nurseries, the molecular clouds, searching for the smaller structures such as pre-stellar cores, outflows and discs. Maser polarization observations are extremely important since they can reveal the morphology and the strength of the magnetic field, probing and mapping the field close to the protostar.
The birth of a star always happens in the darkness of cosmic dust. When a newborn star finally becomes visible at optical frequencies, the formation processes that we are interested in has already stopped. Thus to study the embedded stellar nurseries we need to use a telescope sensitive at the wavelengths where the surrounding material is transparent. This is possible from Earth by observing from the radio to the mm and sub-mm ranges; the required high resolution is obtained with

interferometric observations.
An interferometer such the Multi-Element Radio Linked Interferometer Network (MERLIN), currently updated to eMERLIN, provided the sensitivity and the spatial and spectral resolution needed to detect the signature of protostellar processes at scale of ~ 10 au. In this work I make use of MERLIN data to investigate the magnetic field structure of the hot core IRAS 18089-1722, using 6.7 GHz methanol maser observations.
The structure of this thesis is as follows. I will introduce briefly the SF process in the molecular clouds in Chap. 2. I will describe a basic theory of masers and their importance in the star formation process in Chap. 3. In Chap. 4 the special case of the hot core IRAS 18089-1722 will be described. The key steps of the data reduction are reported in Chap. 5. The main results and future prospects are given in Chap. 6.

Chapter 2

Star Formation

2.1 Molecular clouds

Stars form in condensations of the ISM known as molecular clouds (MCs), whose main component is the H_2 molecule. MCs are among the most massive objects in our Galaxy (up to 10^6 $M_\odot$) and the coldest, with temperatures ranging between 10 and 50 K, with most of the gas at the lower end of the interval. Their densities span several orders of magnitude, from $\sim 10^2$ to $\sim 10^6$ cm^{-3}, and even higher in star forming cocoons.
H_2 however is not easily detected. The reason is that H_2, having a symmetric shape, lacks a permanent dipole moment. It is much easier to observe transitions from CO, which is the second most abundant molecule ($N_{\rm CO}/N_{\rm H_2} \sim 10^{-4}$). CO has a permanent dipole moment, so that total angular momentum $\Delta J = \pm 1$ transitions are allowed, and its rotational levels can be excited by collisions with H_2. For this reason, CO is widely used as a tracer of H_2, though some discussion exists on the actual value of the CO to H_2 conversion factor, $X_{\rm CO}$.
Although H_2 is easily photo-dissociated by UV radiation, if the mass of the MC is large enough, an equilibrium may be established between the H_2 formation and its destruction. The inner regions of a MC are shielded from the ionizing radiation, also due to the presence of dust.
About 1% of the mass of a molecular cloud consists of dust. Dust plays an important role, because the most efficient channel for H_2 production is surface reactions on interstellar grains (Gould & Salpeter 1963; Hollenbach & Salpeter 1971). The presence of dust is also required to explain the abundances of molecules containing heavy atoms, which are too large to be explained if the molecules form only from gas-phase atoms. Dust surface chemistry is indeed considered the most important channel for the formation of H_2O and complex organic molecules.
Other species, especially molecules containing only a few atoms such as CO, CH and CH_4, are thought to form from gas-phase material, without involving catalysis

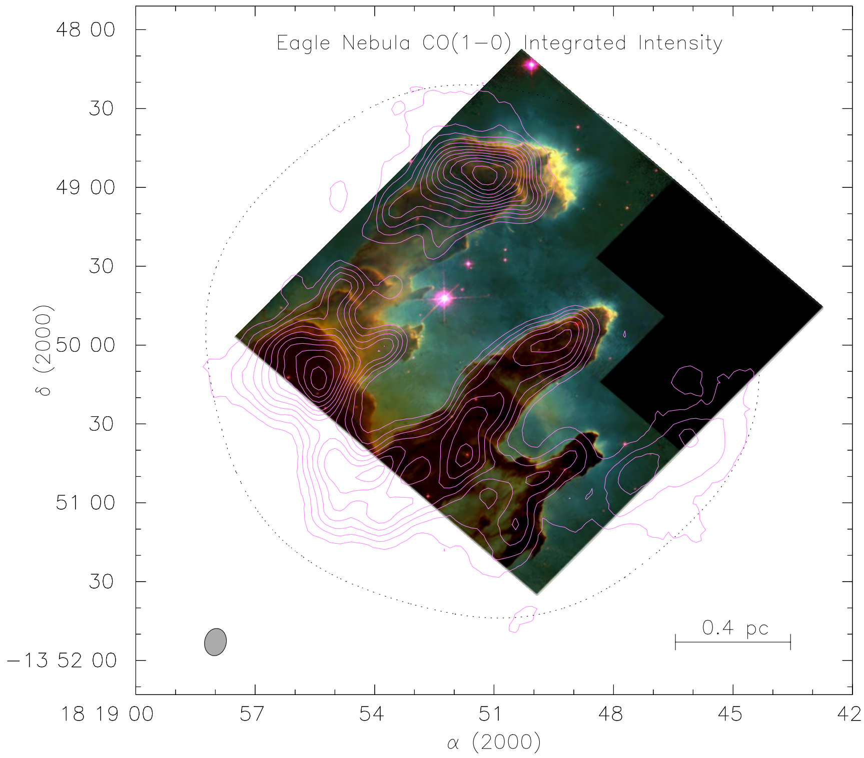

Figure 2.1: Molecular gas in the M16 nebula. The contours show the emission from the CO molecule observed with the BIMA array, superimposed on an optical image from HST. The brown pillars show dense, opaque regions which have not yet been ionized by the strong UV radiation field, and which contain protostellar cores still embedded in the molecular material. The molecular gas distribution, traced by the CO emission, follows very well the brown pillars. The blueish parts of the image are filled with hot, tenuous ionized gas ("blister HII region", see Sect. 2.3.2). Figure from Pound (1998).

by dust. The H_2^+ ion may be produced by cosmic rays carrying enough energy to penetrate a molecular cloud. This ion may bind with an H atom, forming H_3^+, which is the first step for several reactions involving gaseous C, N and O. Further chemical reactions may also take place in shocked, high-temperature regions and/or in photoionized regions, such as those in the neighbourhood of massive stars (see Sect. 2.3).

Radicals, which are highly reactive molecules with unpaired electrons such as OH, CH, CN, HCO^+, plus molecules never detected in terrestrial laboratories (e.g. $HC_{11}N$) are also found in MCs.

The first organic molecule discovered in MCs was formaldehyde (H_2CO, Snyder et al. 1969). Many more have been discovered since then, showing that complex organic molecules (that potentially play a role in the development of life) can form

Table 2.1: Summary of molecular cloud components and their proprieties.

Categories	Mass	Size	n_H
	$M_\odot$	pc	cm^{-3}
GMC Complex	10^5–$10^{6.8}$	25–200	50–300
GMC	10^3–$10^{5.3}$	2–20	10^3–10^4
Clump	10–10^3	0.2–2	10^4–10^5
Core	0.3–10^2	0.02–0.4	10^4–10^6

and survive in the harsh environments of interstellar space.

2.2 Star formation in dense molecular cores

Observations have shown that MCs are found both in isolation or grouped in complexes, forming a giant gravitationally bound group of clouds (giant molecular cloud, GMC). A typical example of GMC complex is the Orion Molecular Cloud located at a distance of ~414 pc from us.
MCs are composed of smaller units ("clumps") with masses between 10–10^3 $M_\odot$, densities between 10^4–10^5 cm^{-3}, radii 0.2–2 pc, and temperatures $\sim$ 10 K (Shu et al. 1987).
The denser parts of MCs within the clumps are known as molecular "cores", and they are the sites where star formation occurs (Fig. 2.1). The typical masses of cores range between 0.3 and 10^3 $M_\odot$, while their densities are usually in the 10^4–10^6 cm^{-3} interval. The radii are between 0.02 and 0.4 pc, and the temperature between 10 and 100 K. In Table 2.1, I present a summary of the cloud components and their properties.

2.2.1 Low-mass star formation: theory

The most widely accepted model describing low-mass star formation shows that low-mass stars form inside gravitationally bound cores, generated during the fragmentation of a MC.
In an idealized simple case, a self-gravitating spherical core of mass M, radius R, density ρ, pressure P and temperature T starts to collapse when its internal gas pressure is not strong enough to sustain gravitational force. The Jeans theory considers only thermal and gravitational effects, from which the Jeans length can be obtained as

$$\lambda_J = c_s \left(\frac{\pi}{G\rho}\right)^{\frac{1}{2}} \propto c_s \tau_{ff} \quad , \tag{2.1}$$

where k is the Boltzmann constant, $c_s = \left(\frac{5kT}{3m_p}\right)^{1/2}$ is the isothermal sound speed,

m_p is the proton mass and τ_{ff} is the free-fall timescale:

$$\tau_{ff} = \left(\frac{3\pi}{32G\rho}\right)^{\frac{1}{2}} \quad . \tag{2.2}$$

The Jeans length represents the scale at which the thermal energy per particle kT balances the gravitational energy GM/R. All scales larger than the Jeans length are unstable. The Jeans mass corresponds to the mass included in a sphere of radius $\lambda_J/2$

$$M_J = \frac{4\pi}{3}\rho\left(\frac{\lambda_J}{2}\right)^3 \quad . \tag{2.3}$$

Under the Jeans theory and with the typical values of molecular clouds such as $c_s = 2\times10^4$ cm s^{-1}, $\rho \sim 10^{-19}$ g cm^{-3}, the Jeans length is $\lambda_J \sim 1.7 \times 10^{18}$ cm $= 0.56$ pc and the typical $\tau_{ff} \sim 10^5$ yr.
A more complete theory should include turbulent velocity inside the core, rotation, and magnetic fields. In general, gravitational collapse is possible if

$$E_{\text{gravitation}} \geq E_{\text{thermal}} + E_{\text{rotation}} + E_{\text{turbulence}} + E_{\text{magnetic}} \quad . \tag{2.4}$$

Assuming a spherical configuration and uniform density, the gravitational energy is

$$E_{\text{gravitation}} = \frac{3}{5}\frac{GM^2}{R} \quad . \tag{2.5}$$

The total thermal energy for an isothermal ideal gas with temperature T is

$$E_{\text{thermal}} = \frac{3}{2}\frac{kTM}{m_u\mu} \tag{2.6}$$

where m_u is the atomic mass unit and μ is the molecular weight of the gas in atomic mass units. The rotational energy, assuming uniform angular velocity ω, is

$$E_{\text{rotation}} = \frac{1}{5}MR^2\omega^2 \quad . \tag{2.7}$$

The turbulent kinetic energy is

$$E_{\text{turbulence}} = \frac{1}{2}Mv^2 \tag{2.8}$$

where v is the mean turbulent velocity. The magnetic energy is

$$E_{\text{magnetic}} = \frac{1}{8\pi}\int_V B^2 dV \sim \frac{1}{6}B^2R^3 \tag{2.9}$$

where B is the assumed uniform magnetic field.

Thus the collapse occurs when the gravity overcomes several barriers, and some conditions are achieved. First, gravitational forces must prevail over the magnetic and the gas pressure. Then, since the collapsing gas experiences extreme compression (from $\sim 10^{18}$ to $\sim 10^{11}$ cm), the density increases drastically (a factor of $\sim 10^{21}$), and the angular momentum must be transferred from the collapsing material to the surrounding cloud. Eventually, the forming protostar must dissipate the magnetic field initially present in the collapsing gas.

The ISM inside a molecular cloud is known to be strongly magnetized. The plasma (composed by electrons, protons, charged dust grains and ions) is deeply coupled to the magnetic field: the magnetic field lines are said to be *frozen* into the fluid and build a net that supports the gas against the collapse. Also, the charged particles circle around the magnetic field lines, colliding with other neutral particles in the surrounding molecular cloud and acting against the collapse. In addition, the magnetic turbulence, which propagates magneto-hydrodynamic Alfvén waves, contributes in counteracting the gravity. Their effects however can't last for long. Phenomena such as *ambipolar diffusion* (Mouschovias 1976; Krasnopolsky & Gammie 2005; Vázquez-Semadeni et al. 2005) and *Ohmic dissipation* (Shu et al. 2006; Gonçalves et al. 2008) operate by dissipating the magnetic flux by several (~ 5) orders of magnitude.

When the fractional ionization is low, as for examples inside a dense MC, the neutral matter is only loosely coupled to the ionized matter. The ambipolar diffusion makes the neutrals decouple from the charged particles; the neutrals, not being bound by the frozen magnetic field, start to collapse under the influence of the gravity. Ohmic dissipation acts similarly, but converting the magnetic energy in thermal energy: some residual coupling still remains and because of this, when the neutrals collapse, the magnetic field lines in opposite directions are pressed together. When the field lines reconnect, energy is released in form of heat.

However, it is not yet clear which process dominates between Ohmic dissipation and ambipolar diffusion; it probably depends on the magnitude of the initial magnetic energy density relative to the gravitational and turbulent energy density and the initial magnetic field configuration. In a cloud with density $n_H \gtrsim 10^6$ cm^{-3} the timescale for ambipolar diffusion and the gravitational free-fall are almost of the same order of magnitude ($\sim 10^6$ yr), but when the density increases the gravitational free-fall time becomes longer than the ambipolar diffusion time, meaning that the ambipolar diffusion may produce the magnetic flux loss in a collapsing clump.

As the collapse proceeds, the gas accumulates and deforms the magnetic field towards the centre of the core, generating a hourglass shape, as observed for instance in the case of the low mass protostar system NGC 1333 IRAS 4A (Girart et al. 2006).

If the angular momentum is conserved then the contraction cannot occur. Thus the angular momentum must be transferred from the collapsing gas to nearby material

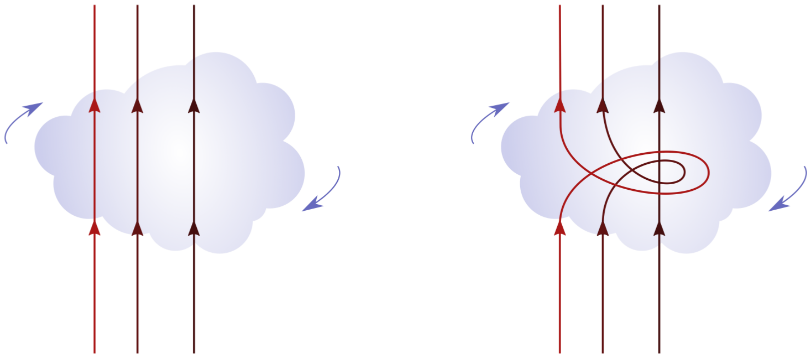

Figure 2.2: Schematic description of how the cloud core rotation can distort the magnetic field lines. Torsional twists travelling along the field lines at the Alfvén velocity can carry away angular momentum excess.

which disposes itself in a protostellar disc. The angular momentum removal can result from two mechanisms: the gravitational torques and the magnetic torques. The first one operates when the density field in the collapsing area presents asymmetries around an axis. Spiral waves in the disc can be observed as an effect of the torque applied by the gravitational field. The typical timescale is of the order of the dynamical time

$$\tau_{dyn} \propto \frac{1}{(4\pi G\rho)^{\frac{1}{2}}} \quad . \tag{2.10}$$

Under the effect of a non-uniform rotation caused by the ongoing collapse, an inevitable twisting of the magnetic fields lines, tied to the larger Galactic magnetic field, appears when the gas starts to condense along them. In order to simplify the geometry, we are assuming that the rotation axis is parallel to the direction of the magnetic field direction. The magnetic torques arise generating the *magnetic braking* which transfer the angular momentum to the matter along the equatorial plane creating a rotating disc. Fig. 2.2 illustrates how the cloud core rotation can distort the magnetic field lines. Torsional twists travelling along the field lines at the Alfvén velocity can carry away angular momentum excess. The typical timescale for the magnetic braking is of the order of

$$\tau_{mb} \propto \frac{1}{\sqrt{GM/R^3}} \quad , \tag{2.11}$$

that reduces to the dynamical time (Eq. 2.10), when the magnetic energy is comparable to the gravitational energy.

Meanwhile the protostar accretes material from the parental MC through the accretion disc: the gas from the surrounding envelope falls onto the accretion disc and then it is funnelled onto the protostar. But not all the accreting material from the disc reaches the protostar. A significant portion is launched from the poles of the star in high-speed collimated jets, and another portion is ejected via open wide outflows starting from the plane of the disc and often hourglass shaped. Jet phenomena can be originated by magnetically-driven and collimated disc winds (the models involve magnetic field lines and different regions of the disc, and centrifugal forces that can launch material). The jet can remain collimated after quite long distances thanks to MHD and it can present a structure composed by a series of knots (rather than a continuous beam) because of density discontinuities of the envelope or because of non-steady accretion (that implies a variable ejection). Jets are surrounded by a cocoon of pressurized gas (coming from old jets and other material swept up from the environment).

The jets and the outflows are pushed into the surrounding environment injecting angular momentum ($\sim 2/3$ of the disc angular momentum can be carried away) and energy, influencing distances from 1 au to 10 pc away. For this reason outflows and jets (especially in the case of high mass protostar) can retard SF processes. Indeed they can interact with both the envelope (also at far distances from the source) and the core. They can modify the distribution and the kinematics of the dense gas surrounding the protostar (e.g. by constraining the infalling envelope to a limited volume outside the outflow lobes, or potentially dispersing the circumstellar envelope (that is the end of the accretion process).

Jets and outflows are also sources of turbulence, not only in the cloud but also in the core. They can reshape the structure of the SF core by sweeping and cleaning the surrounding dense gas and producing density enhancements along the outflow axis. They can also potentially be able to disperse the entire core.

The energy released by outflows and jets can heat the cloud via shock interaction generated by the propagation of the wind through the surrounding medium. The consequent series of heating and compression of the material alter the chemistry of the cloud and can also affect the future SF process in the cloud. The chemistry laboratory involves several molecular reactions, dust disruption and ice mantle sublimation. A comprehensive review of these processes can be found in Arce et al. (2007).

Finally, also the formation of multiple systems and binaries can help the dissipation of the initial angular momentum, which is transferred to the orbital motion of the stars. This scenario is supported by empirical evidence that $\sim 2/3$ of the F and G type stars are in multiple systems (Duquennoy & Mayor 1991; Kouwenhoven et al. 2009).

2.2.2 Low-mass star formation: observations

Shu et al. 1987 identified five stages for the collapse and the formation of a low-mass star. This phases can be observationally distinguished by the emerging spectral energy distribution (SED), in five classes (see Fig. 2.3), as shown by Lada (1987) and André (2002). Following these authors, I present here a short and essential summary of the phases and the corresponding classes.

I) A slowly-rotating cloud core forms.

II) The core passes the brink of instability and collapses "inside-out", i.e. starting from the inner denser part; this phase is characterized by a central protostar, surrounded by an accretion disc, both embedded in an envelope of infalling material. This is the main accretion phase, known as *hot corino* phase. The object is highly extincted, only emitting at sub-mm wavelengths. The continuum spectrum is a blackbody with very low temperature (Class 0). Infall signatures may be found in the spectrum.

III) Deuterium ignites in the protostar, which develops convection and a stellar wind. As the infalling material falls preferentially on the disc, the wind may break through the rotational poles and develop collimated jets and a bipolar outflow. An IR excess is developed (Class I).

IV) The wind widens its opening angle, revealing a T-Tauri star surrounded by a disc. The emission is peaked at IR or visible wavelengths (Class II).

V) The disc disappears, either incorporated in companion bodies, or dispersed by radiation. The emission peaks at visible or IR wavelengths, consistent with a reddened stellar photosphere of a young star with little or no circumstellar material (Class III).

2.3 High-mass star formation

High-mass stars are commonly defined as stars with mass $\geq$8 $M_{\odot}$, and they play a fundamental role in the evolution of the universe. They radiate a considerable amount of UV radiation, emit strong wind and shocks, reshape and enrich the gas reservoir and they dominate the starbust activities in galaxies. However, our understanding of the physical process involved in the formation of massive stars is still incomplete, and this lack of knowledge still prevents us from building a clear picture of the early evolutionary stages of the high mass protostars.
Observationally, the identification of high mass protostars is extremely complicated, more than their low-mass counterparts, since they are rare and they evolve quickly ($\sim 10^5$ yr). Protostellar cores are embedded in dark clouds, typically located at fairly large distances from us. They often form in dense clusters where

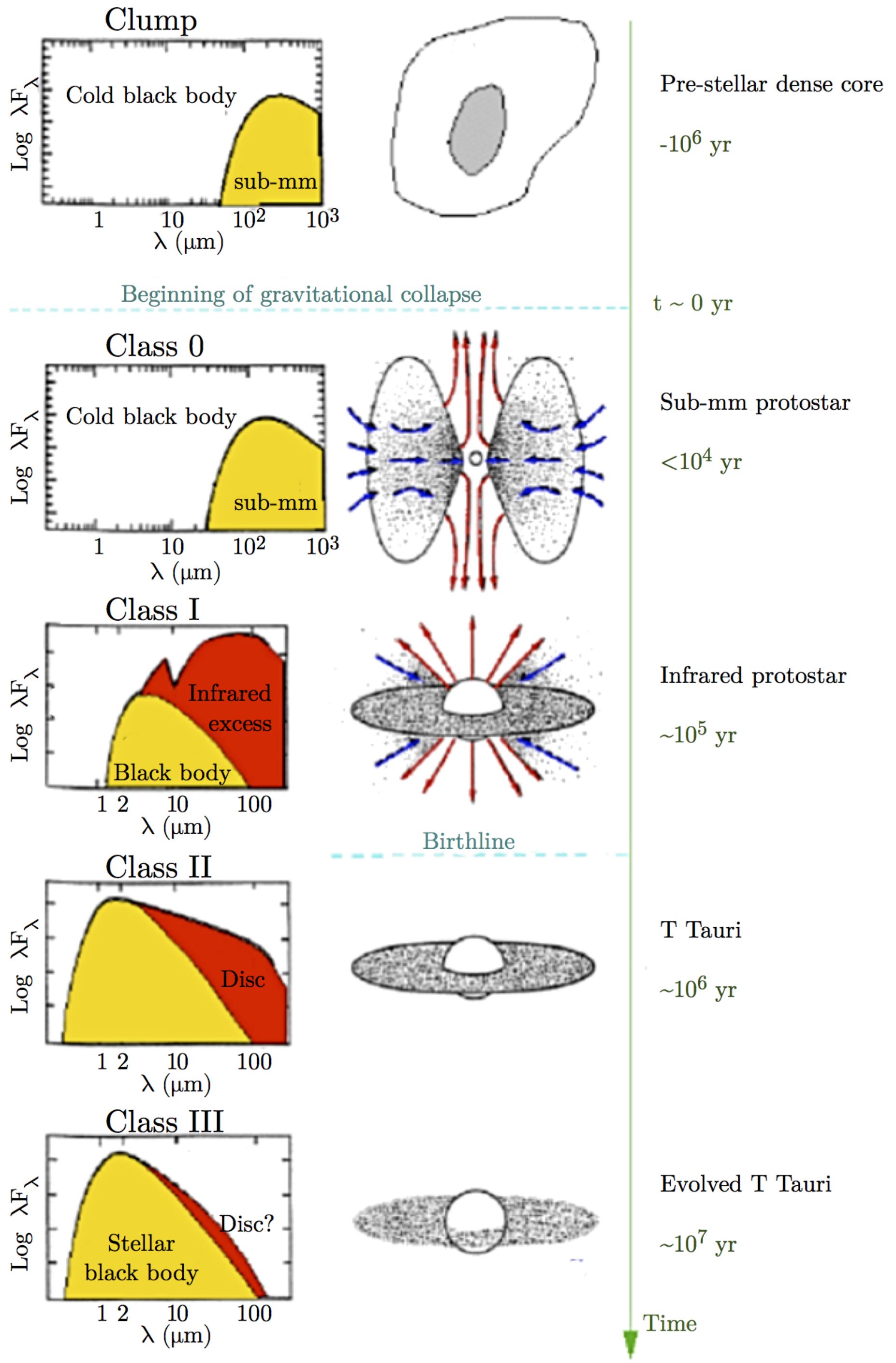

Figure 2.3: Infrared/Submillimiter Young Stellar Object Classification (Lada 1987; André et al. 1993; André 2002): SED classes and evolutionary steps for the low-mass star formation.

the cores are only separated by few arcsecs, making it more difficult to study the effects and influences of single and isolated stars separately. Moreover high-mass stars start to burn hydrogen before the conclusion of the accretion stage, resulting in a further challenge in disentangling the intrinsic luminosity of the protostar from the luminosity due to the accretion.

As a consequence, the high-mass star formation theory falls behind the low-mass one. Furthermore, the theories that have been proposed are matter of some debate.

2.3.1 High-mass star formation: theory

To explain the formation of high mass stars, theories have to face two main problems: the time-scale problem and the radiation pressure problem. The Kelvin-Helmholtz time is the ratio of potential energy to luminosity

$$\tau_{KH} = \frac{GM^2}{RL} \propto 3 \times 10^7 \left(\frac{M_*}{M_\odot}\right)^2 \left(\frac{R_*}{R_\odot}\right)^{-1} \left(\frac{L_*}{L_\odot}\right)^{-1} \quad \text{yr}, \tag{2.12}$$

and it provides an indication of how fast the collapse will be for a star without nuclear energy supply. M_*, L_* and R_* are the final mass, luminosity and radius of a star. In the case of a low mass star, like the Sun, the thermal evolution is governed by the Kelvin-Helmholtz time which is of the order of $\tau_{KH} \sim 10^7$ yr. The typical accretion rate for a low mass protostar is $\dot{M} \leq 10^{-7}\ M_\odot\ \text{yr}^{-1}$, which means that to accrete 1 $M_\odot$, an accretion time $t_{accr} = M/\dot{M} \sim 10^7$ yr is needed. Since the $t_{accr} \sim \tau_{KH}$, a Sun-like star starts the nuclear burning in the core when the accretion is ended.

For a high mass protostar generating a massive star of about 60 $M_\odot$ and 12 $R_\odot$ and $10^{5.9}$ $L_\odot$, the Kelvin-Helmholtz time is $\tau_{KH} \sim 10^4$ yr. Considering an accretion rate of $\dot{M} \leq 10^{-4}\ M_\odot\ \text{yr}^{-1}$, we need an accretion time $t_{accr} \sim 10^6$ yr. So $\tau_{KH} < t_{accr}$, which means that a small hydrostatic core starts to burn hydrogen at the centre, while the massive protostar is still accreting. The resulting nuclear burning generates luminosity and consequently radiation pressure that counteracts the accretion of gas. Moreover the Eddington luminosity, which is the maximum reachable value of the luminosity before the radiation pressure starts to blow away the infalling gas, sets a limit on the mass. Assuming spherical symmetry and a fully ignited H core, and considering the mass-luminosity relationship for protostars, it seems impossible to form masses $> 10\ M_\odot$ due to the radiation pressure action. Despite that, massive stars are observed and therefore there must be some physical process not yet understood allowing their formation. Currently there are two most important scenarios being debated: the core accretion model and the competitive accretion model.

Core accretion model

The fundamental idea of the core accretion model (McKee & Tan 2003) is that low mass and high mass stars form similarly, through fragmentation of the parental cloud under the action of magnetic fields, self-gravity and turbulence. Each core or corino evolves alone. Simulations have shown that, for low angular momentum, the gas accretes directly, while for high angular momentum, the accretion goes via disc. This model can explain the formation of massive stars since the accretion is supported by turbulence, giving an accretion rate of

$$\dot{M} \sim 0.5 \times 10^{-3} \left(\frac{M_*}{30M_\odot}\right)^{\frac{3}{4}} \Sigma_{\rm cl}^{\frac{3}{4}} \left(\frac{M}{M_*}\right)^{\frac{1}{2}} \quad M_\odot \ {\rm yr}^{-1}, \tag{2.13}$$

and a time-scale for accretion of the order of

$$t_{accr} \sim 1.3 \times 10^5 \left(\frac{M_*}{30M_\odot}\right)^{\frac{1}{4}} \Sigma_{\rm cl}^{\frac{3}{4}} \quad {\rm yr}, \tag{2.14}$$

where $\Sigma_{\rm cl} \sim 1$ g cm^{-2} is the clump surface density. Under this scenario the velocity dispersion and the core density are power law functions of radius. The core is supported by turbulence which provides enough ram pressure to prevent the collapse at each radius. To form a massive star of $100M_\odot$, the final accretion rate is $\dot{M} \sim 10^{-3} M_\odot$ yr^{-1} and the $t_{accr} \sim 1.7 \times 10^5$ yr.

There is smooth accretion up to ~ 17 M$\odot$. Over this value, the radiation pressure drives out gas and forms bubbles, meanwhile the outflow arises blowing away the material along the polar axis. In this way, since most of the radiative flux can escape from the outflow cavities (flashing effect), the radiation pressure can be finally overcome. Eventually, the strong UV radiation emitted by the young massive star can ionize and evaporate the surrounding disc limiting the accretion, and can reach the adjacent zone generating an HII region.

From the core accretion model we can obtain a direct relation between the Core Mass Function (CMF; it tells us for a given cloud mass how many big/small cores are formed) and the Initial Mass Function (IMF; it tells us the same of CMF, but for the mass of the stars, how many high/low mass stars are formed). The model also suggests that the amount of the gas of the MC which forms stars is small, and it is proportional to how much gas is gravitationally bound to the cloud.

Some criticism to the core accretion model could be posed by asking why massive stars are not found in isolation but always in clusters (OB associations). One possible answer could be that the turbulence creates density fluctuations and induces the fragmentation in smaller cores, but this would be opposed by the magnetic field which should instead prevent the fragmentation.

Competitive accretion model

The principal differences between the core accretion scenario and the competitive accretion (Bonnell & Bate 2006) are the gas reservoir and the accretion process. In the core accretion model the mass reservoir is the core itself and it is gathered before the accretion via disc begins. For competitive accretion, the mass is instead collected during the star formation process from the entire cloud and the accretion is spherical (Bondi-Hoyle accretion).

The competitive accretion model is based on two main concepts (Zinnecker & Yorke 2007). The first one says that the *location* is important: the environment can influence significantly the process of growth. The protostar's ability to grow depends on the site of its accretion domain, so when the protostar is at the centre of a protostellar cluster, this means that the accretion domain is the whole cloud. The second concept is *the rich get richer*: the more massive is the protostar, the more successful the gravitational accretion. There is a tidal capture of material, since the star accretes while moving through the uniform gas of the cloud, at a rate given by the Bondi-Hoyle accretion rate

$$\dot{M}_{\mathrm{B-H}} = 4\pi\rho \left(\frac{GM}{c_s^3}\right)^2 \quad . \tag{2.15}$$

This scenario implies the preferential formation of massive stars in dense environments, while low mass stars can form alongside in the less dense zones of the cloud. No isolated high mass protostars are predicted by this model but only stars in gravitationally bound clusters. The magnetic field is not involved in the process and doesn't support the gas which moves freely in the cloud.

Critics to this scenario ask how stars with masses $> 10\mathrm{M}_\odot$ can be formed, since the spherical accretion is stopped by the radiation pressure. One solution could be a global gravitational collapse occurring simultaneously in the entire clump where the formation process is undergoing.

2.3.2 High-mass star formation: observations

The main empirical evolutionary phases characterizing high mass protostars are four as shown in Fig. 2.4: infrared-dark clouds (IRDC), hot molecular cores, and HII regions, divided in hyper-compact and ultra-compact HII regions.

I) The IRDC phase is the earliest empirical evolutionary step for high mass star formation. The gas here is optically thick at infrared wavelengths ($\sim 1-10\mu$m), the mass range can vary between 100-1000 $\mathrm{M}_\odot$, and the typical temperatures of an IRDC are around 10-20 K. Inside IRDCs it is possible to recognize dense, cold cores with masses of up to ~ 100 $\mathrm{M}_\odot$ and densities of up to $\sim 10^6\mathrm{cm}^{-3}$. Within the cores the gas starts to collapse.

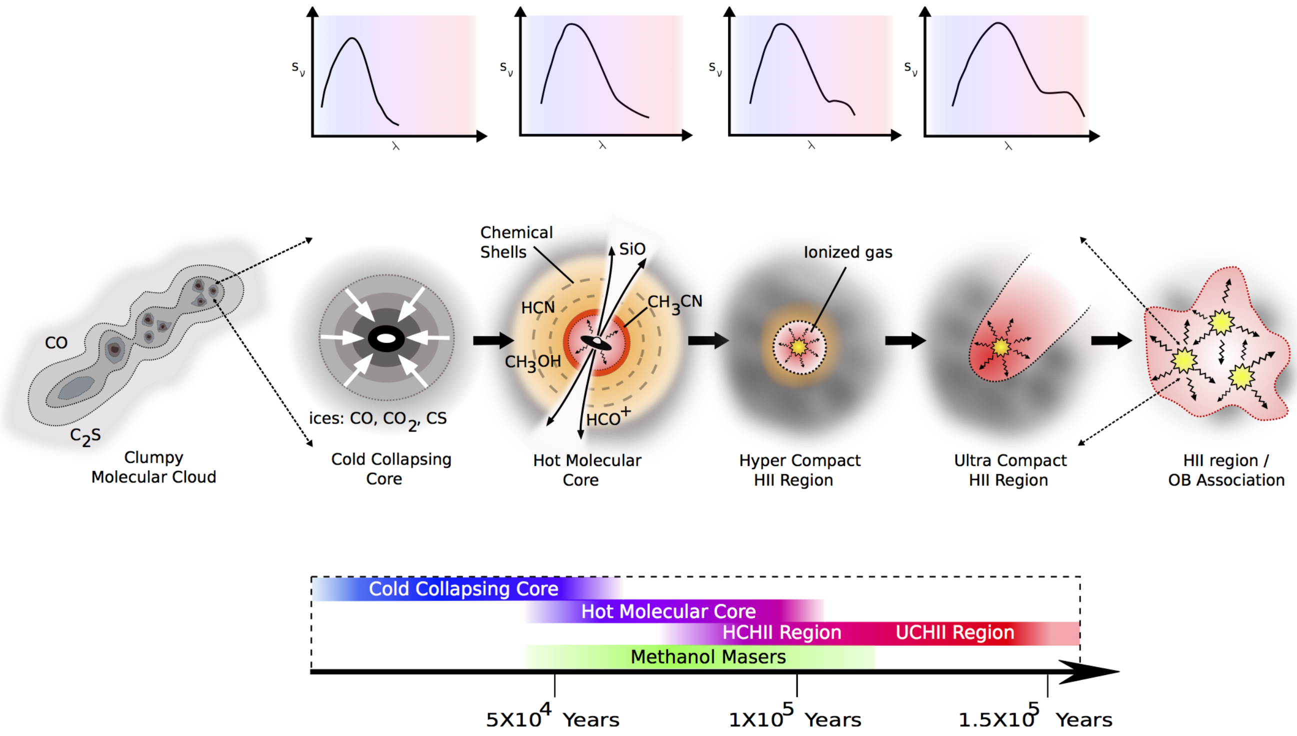

Figure 2.4: This sketch delineates the evolutionary sequence for an association of high-mass protostars, showing the typical steps and spectral classes on the basis of the current observations (Credit: Dr Cormac R. Purcell - University of Sydney).

II) During the hot molecular core phase the star formation process has just started: after the collapse of the cloud, matter falls inward and feeds the protostellar object inside. Gravitational energy is released as radiation, and the matter at the centre of the infalling envelope warms up.

The envelope of this type of sources can be described by two zones. The outer part of the envelope, where the dust temperature is $\leq$100 K, presents a chemistry very similar to that in the pre-stellar core. In this cold region many molecules are frozen onto the grain mantles. The inner part, where the temperature is $\geq$100 K, is called hot core. It is inside this warm and dense region that it is possible to find an onion-like structure, where each shell presents a typical and very active chemistry: since the grain mantles sublimate, all the "dirty ice" components are injected into the gas phase and start to react in a steady series of "parent-daughter" reactions. This possible scenario is shown in Fig. 2.5, and the model proposed by Awad et al. (2010) also suggests that the chemical activities are similar in both hot cores and in their lower mass counterparts, hot corinos.

III) The HII region phase begins when the protostar ignites and the newly formed

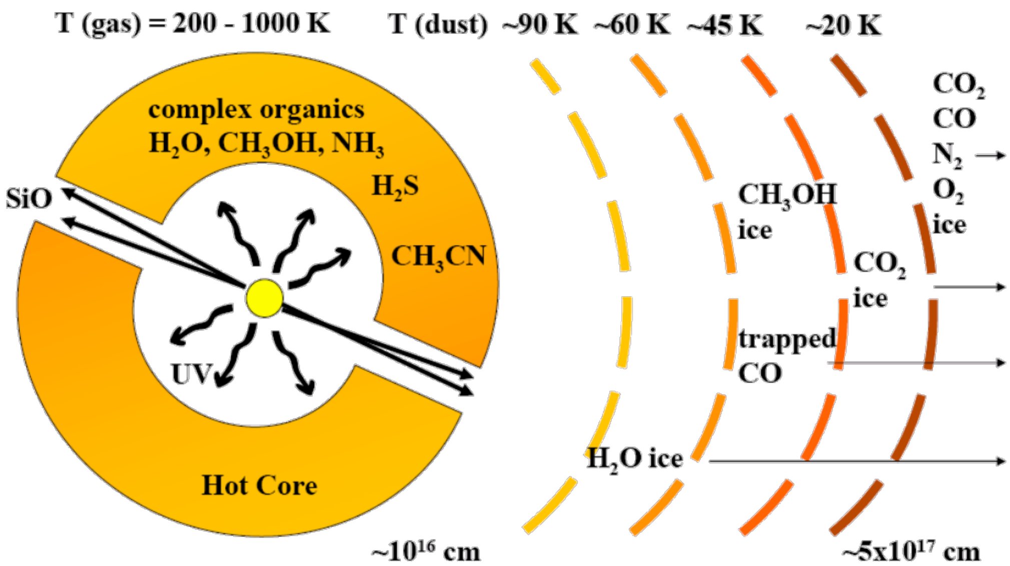

Figure 2.5: A schematic view of a hot molecular core and colder shells. The hot molecular cores are OB star nurseries, which are larger and more massive than the hot molecular corinos. The physical differences between the two object are listed in Table A below. Figure and Table A from Beltran (2011).

Table A. Physical characteristics of Hot Molecular Cores and Corinos

Source	Temperature K	Luminosity $L_\odot$	Density cm^{-3}	Size AU
Hot Core	>100	$>10^4$	$\sim 10^7$	$<2\times10^4$
Hot Corino	>100	$>10^4$	$\sim 10^8$	<150

star starts to ionize its surroundings. Typically OB stars are very luminous ($L \geq 10^4 L_\odot$), hot ($T_{eff} \geq 20000$K) and are grouped together forming an OB group or association. They emit a large amount of UV radiation which leads to the ionization and heating (to temperatures of $\sim 10^4$ K) of the gas volume around them. This ionized bubble is known as an HII region, and the resulting high pressure causes the expansion of the ionized bubble.

Where radiation hits the molecular cloud it creates a thin layer of ionized material, called ionization front, which progresses into the cloud. In Figs. 2.6 and 2.7, ionization fronts in the M16 and G353.2+0.9 HII region are clearly visible. The energy released in the ionization front warms the material, so the pressure rises. A shock is driven into the molecular cloud, compressing its material, reshaping the environment by creating edges, pillars and amazing shapes. The compressed layer may become unstable and fragment, forming dense cores which eventually may collapse and form stars (e.g., Hester & Desch 2005).

Examples of this process at work are seen in M20 (Lefloch & Cernicharo 2000), W5 (Karr & Martin 2003), RCW97 (Zavagno et al. 2006), and Sh2-217 (Brand et al. 2011). Also, water masers (linked to class-0 protostars) in M16 are concentrated in the compressed regions just beyond the shock (Healy et al. 2004).

Compact HII regions are small areas of ionized gas that surround newly formed high-mass stars. Ultra-compact HII (UCHII) regions have usually sizes between 0.01 and 0.1 pc and densities $\geq 10^{16}$ cm^{-3}, while the hyper-compact HII (HCHII) regions present sizes $\leq$0.01 pc and densities $\geq 10^{18}$ cm^{-3}). UCHII regions are usually taken to have a size between 0.01 and 0.1 pc. Since massive stars quickly burn the H in the centre, the typical main-sequence lifetime of an OB star is $\leq 3 \times 10^7$ years. Therefore HII regions are concentrated near sites of recent and on-going star formation, such as giant molecular clouds or in the spiral arms of the galaxies.

2.4 Magnetic Fields

Magnetic fields play an important role in the dynamics of molecular clouds. Considering the ratio between the flux of the magnetic energy Φ and the mass of a cloud M$_C$ (assumed spherical) we can see that the magnetic pressure can inhibit the collapse of the cloud only if

$$\frac{\Phi}{M_C} > \left(\frac{\Phi}{M}\right)_{crit} = 3\pi\sqrt{\frac{2aG}{5b}} = 1.54 \times 10^{-3}\sqrt{\frac{a}{b}}\ \mathrm{G\,cm^2\,g^{-1}} \quad , \tag{2.16}$$

where a and b are proportionality constants that can be obtained from numerical simulation (Mouschovias & Spitzer 1976). If $a \sim 1.67$ and $b \sim 1.25$, then $(\frac{\Phi}{M})_{crit} = 1.8 \times 10^{-3}$ G cm^2 g^{-1}. This means that only magnetically supercritical masses, with $\frac{\Phi}{M_C}$ less of the critical value, are able to undergo gravitational collapse. By observing the magnetic field strength B and the column density $N(H_2)$ in star forming regions, it is possible to estimate the ratio between the flux of the magnetic energy and the mass of the cloud, $\frac{\Phi}{M_C} \propto \frac{N(H_2)}{|B|}$. The Zeeman effect is the main tool to measure the magnetic field, or at least its component along the line of sight. In a survey of 66 HI clouds and 72 molecular clouds, Crutcher et al. (2010) found median field strengths $B \sim 5$ μG or 49 $\left(\frac{n_H}{10^4\mathrm{cm}^{-3}}\right)^{0.65}$ μG, for densities n_H lower or higher than 3×10^2 cm^{-3}, respectively.
In the case of density higher than the above threshold, a median Alfvén speed $v_A = B/\sqrt{4\pi\rho} \sim 0.90 \left(\frac{n_H}{10^4\mathrm{cm}^{-3}}\right)^{0.15}$ km s^{-1} is implied.
The importance of the magnetic field can be also assessed by taking the ratio between the magnetic energy density $B^2/8\pi$ and the kinetic energy density $\frac{1}{2}\rho\sigma_v^2$,

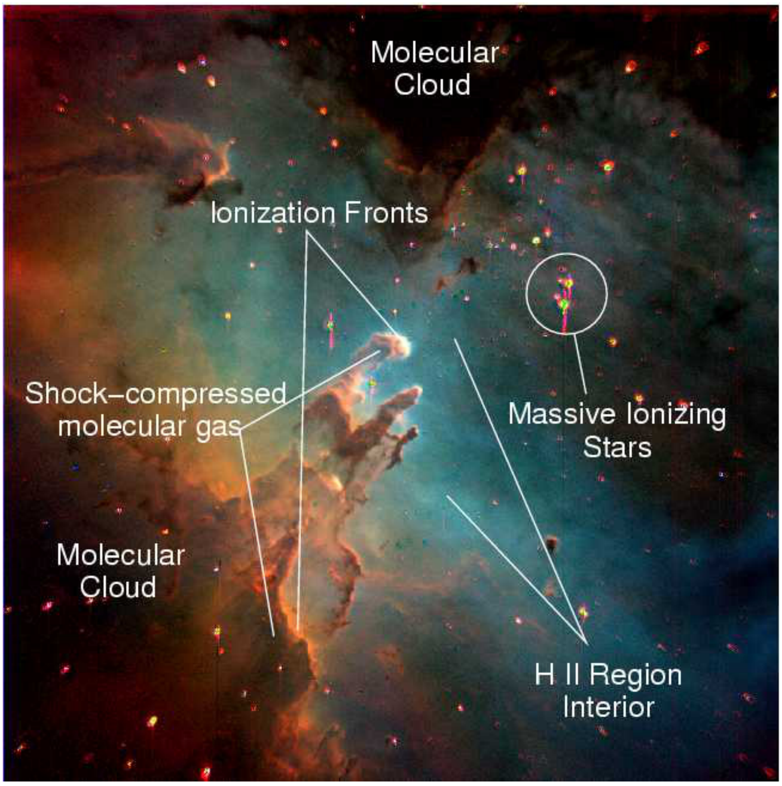

Figure 2.6: The M16 nebula, prototype of a blister HII region. The interior of the HII region is a cavity of hot ($T \sim 10^4$ K), tenuous ($n \leq 10^2$ cm^{-3}) gas that is being photoionized by EUV radiation from a number of massive stars. The HII region is partially surrounded by a molecular cloud. In some locations the molecular cloud can be seen as dark regions against the bright background of the nebula. Most of the EUV radiation from the massive stars is absorbed in ionization fronts seen at the interface between the HII region and the molecular gas (Hester & Desch 2005).

where σ_v is the velocity dispersion. This ratio reduces to $(v_A/\sigma_v)^2$ whose median value is $0.75\left(\frac{n_H}{10^4 \mathrm{cm}^{-3}}\right)^{0.46}$.

Aligned dust grains offer a second way to measure the strength of the magnetic field, because elongated grains align generally with their short axis parallel to the magnetic field. Linearly polarized emission can be observed from both the dust itself or from background stars whose light passes through the cloud.

The Chandrasekhar-Fermi (CF) method for measuring the magnetic field strength relies on the following idea, that turbulence in the cloud may distort the direction of polarization, unless the magnetic field is strong enough that the alignment of dust grains is not significantly disturbed.

Despite several observations that confirm the presence of magnetic field in molecular clouds, its role in the high mass star formation is still poorly understood.

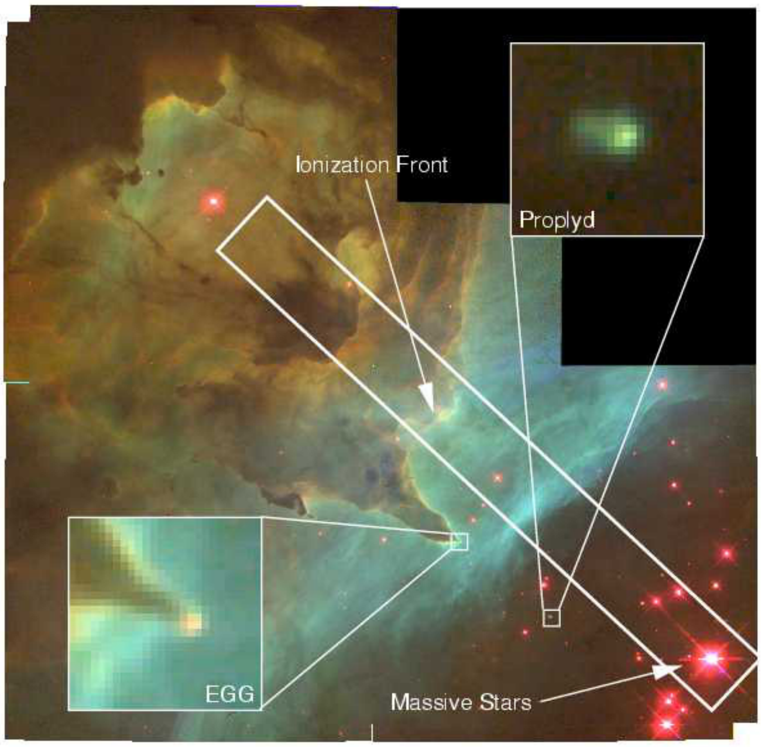

Figure 2.7: The G353.2+0.9 HII region in NGC 6357, in an image taken with the *HST* WFPC2 camera (Healy et al. 2004). The massive star driving the ionization is visible in the bottom right edge.

Computer simulations have shown that the magnetic field can prevent fragmentation around massive protostars, influence accretion and drive collimated outflows and jets. However, theoretical models require more observational constraints on magnetic fields to properly probe their impact on the high mass star formation process (Tan et al. 2014). For example, Seifried et al. 2015 pointed out that some observed morphologies can only be explained by considering detailed and specific magneto-hydrodynamic (MHD) configurations, yet to be tested observationally. A typical case is the rotating disc observed around massive protostars (e.g. Beltrán & de Wit 2016).Only taking in account non-ideal MHD effects such as ambipolar diffusion and Ohmic dissipation or the combined influence of both of them, it is possible to overcome the apparent discrepancy between observations and simulations.
The best way to solve this puzzle is to observe the magnetic field strength and orientation at the small scale of the core centre ($\sim 100-1000$ au). This is possible using masers, which will be the topic of the next Chapter.

Chapter 3

Astrophysical Masers

Microwave Amplification by Stimulated Emission of Radiation (MASER) is based on the concept of *stimulated emission* from quantum theory, introduced by A. Einstein in 1917. The first maser device was developed in laboratory only in 1954 by J. Gordon, H. Zeiger and C. Townes, while the first astronomical observation was obtained by Weaver et al. (1965).

A simple representation of the phenomenon is shown in Fig. 3.1: a photon of wavelength λ is incident on an atom or a molecule presenting already the electrons in an excited energy state (panel a). The photon is not absorbed by the molecule but instead it stimulates an excited electron to decay in a lower energy state, by emitting another photon of identical wavelength λ and phase (panel b). The stimulated emission can amplify the signal coming from an originally weak source. The two photons indeed can stimulate emission from other two molecules (panel c) and the process continues causing a chain of reactions that doubles the number of photons each time (panel d). When all the molecules simultaneously decay to the lower energy levels, the maser occurs generating a narrow and bright beam of coherent and monochromatic light (panel e). The radiation intensity rises exponentially and propagates where the molecules present the same velocity, until the upper level begins to depopulate, and eventually the amplification saturates.

3.1 Basic theory

In order to understand how the stimulated emission works, we can start considering the simplest case of a molecule with only two discrete energy levels, upper (u) and lower (l).

The Boltzmann equation

$$\frac{N_u}{N_l} = \frac{g_u}{g_l} \frac{e^{-\left(\frac{E_u}{kT}\right)}}{e^{-\left(\frac{E_l}{kT}\right)}} \tag{3.1}$$

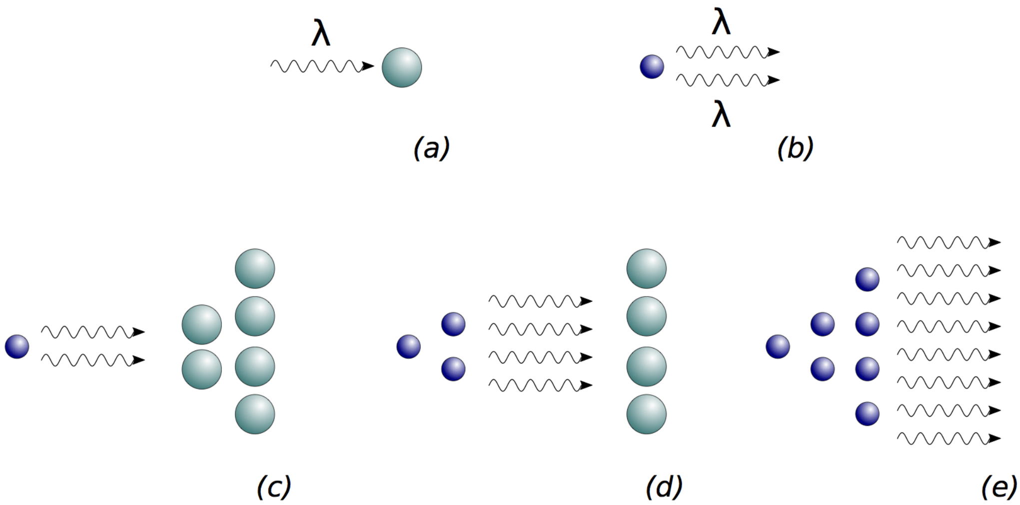

Figure 3.1: Stimulated emission is the physical process motivating masers. In this figure a schematic view of the amplification of the radiation starting from a incident photon on an excited molecules (a) which stimulates the emission of an identical photon (b) and generates a chain of reactions (c-e) causing the maser (see Chap. 3).

is valid under thermodynamic equilibrium, and it gives the ratio between the electron population (N) in the two energy states E, where g are the statistical weights of the two levels, and T is the temperature and k is the Boltzmann constant.
In environments such as the cold and dense interstellar clouds, the Boltzmann formula predicts $N_l \gg N_u$. Therefore to make the stimulated emission occur, an efficient external source of energy must be present, exciting (*pumping*) the gaseous environment and causing the overpopulation of the upper level of a molecular transition (*population inversion*). Thus the pumping puts the gas in a non-equilibrium state, necessary for the maser amplification, where

$$\frac{N_u}{g_u} > \frac{N_l}{g_l} \quad . \tag{3.2}$$

Embedded young stellar objects offer several pumping mechanisms from which the maser may arise: stellar wind and the associated shocks, or far-infrared radiation from heated dust as much as jets and outflows may provide the energy and the right conditions to stimulate emissions from many different molecular species (e.g. H_2O, OH, CH_3OH and SiO).
A more general description must consider the interactions between different energy levels not directly involved in the maser emission, as shown in Fig. 3.2. Π_u and Π_l are the pump rate, defined as number of additional molecules transferred into

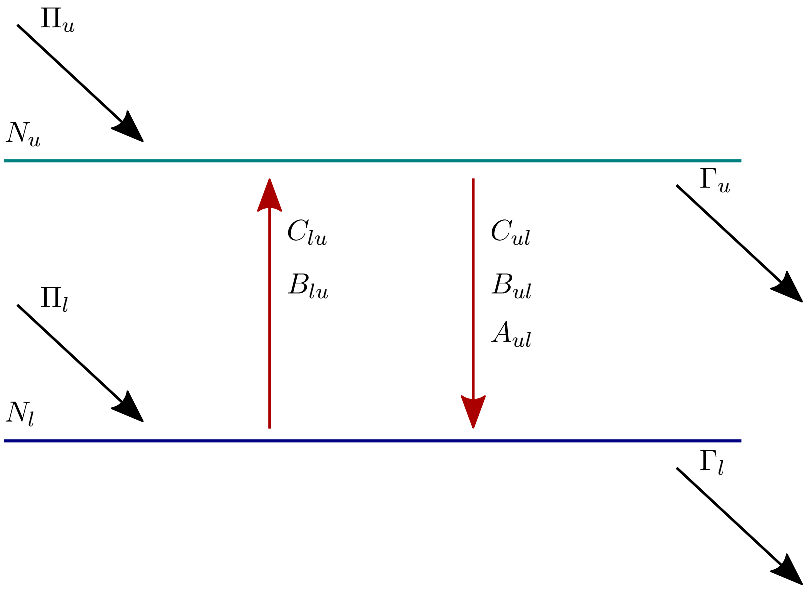

Figure 3.2: Physical processes shuffling the energy level populations in a maser transition (see Chap. 3.1).

the upper and the lower energy level per unit of time and volume, while Γ_u and Γ_l mark the decay rate. The pump efficiency of the population inversion process is

$$\eta = \frac{\Pi_u - \Pi_l}{\Pi_u + \Pi_l} \quad . \tag{3.3}$$

The molecules in the neighbourhood also contribute to the population exchange through inelastic collisions that transfer electrons from the lower to the upper energy level with a rate C_{lu} and from the upper to the lower with a rate C_{ul}. The total rate equations for each level assuming a steady state are:

$$0 = \Pi_u - N_u\Gamma_u - (N_uB_{ul} - N_lB_{lu})J_\nu - N_uC_{ul} + N_lC_{lu} - N_uA_{ul} \tag{3.4}$$
$$0 = \Pi_l - N_l\Gamma_l - (N_uB_{ul} - N_lB_{lu})J_\nu - N_uC_{ul} + N_lC_{lu} + N_uA_{ul} \tag{3.5}$$

where A_{ul} and B_{ul} are the Einstein coefficients for spontaneous and induced emission respectively, and B_{lu} for absorption. J_ν is the angle-averaged maser intensity as a function of the frequency:

$$J_\nu = I_\nu \frac{\Delta\Omega}{4\pi} \quad , \tag{3.6}$$

where the intensity I_ν comes from the equation of the radiative transfer:

$$\frac{dI_\nu}{ds} = -\kappa_\nu I_\nu + \epsilon_\nu \quad . \tag{3.7}$$

κ_ν is the absorption coefficient

$$\kappa_\nu = (N_l B_{lu} - N_u B_{ul})\phi(\nu)\frac{h\nu}{4\pi} \quad , \tag{3.8}$$

and ϵ_ν is the emission coefficient

$$\epsilon_\nu = N_u A_{ul}\phi(\nu)\frac{h\nu}{4\pi} \quad , \tag{3.9}$$

$\phi(\nu)$ defines the line profile function.
From Eqs. (3.4 and 3.5), the general population acting in the maser, assuming that $\Gamma_u = \Gamma_l = \Gamma$ and $N = (\Pi_u + \Pi_l)/\Gamma$, is

$$N_\nu = N_{u\nu} + N_{l\nu} = N\phi(\nu) \tag{3.10}$$

while the population difference is

$$\Delta N_\nu = N_{u\nu} - N_{l\nu} = \frac{\Pi_u - \Pi_i}{\Gamma + 2B_{ul}J_\nu}\phi(\nu) = \tag{3.11}$$

$$= \frac{\Delta\Pi/\Gamma}{1 + 2B_{ul}J_\nu/\Gamma}\phi(\nu) = \frac{\Delta N_0}{1 + J_\nu/J_s}\phi(\nu) = (N_u - N_l)\phi(\nu) \quad . \tag{3.12}$$

where

$$J_s = \frac{\Gamma + (1 + g_u/g_l)C_{ul}}{(1 + g_u/g_l)B_{ul}} \quad . \tag{3.13}$$

The pump efficiency in Eq. (3.3) can be written as

$$\eta = \frac{\Delta N_0}{N} \quad . \tag{3.14}$$

From Eqs. 3.12 and 3.8 we can obtain the maser absorption coefficient

$$\kappa_\nu = -\frac{\kappa_{0\nu}}{1 + J_\nu/J_s} \quad , \tag{3.15}$$

with $\kappa_{0\nu} = \Delta N_0 g_u B_{ul} h\nu\phi(\nu)/4\pi$.
If the angle-averaged intensity is $J_\nu < J_s$, such as at the beginning of the amplification mechanism, the maser radiation doesn't affect the population distribution

between the level and the maser absorption coefficient is $\kappa_\nu = -\kappa_{0\nu}$. Under this case, the maser is called *unsaturated* and from Eq. (3.7) we can obtain

$$\frac{dI_\nu}{ds} = \kappa_{0\nu} I_\nu + \epsilon_\nu \quad , \tag{3.16}$$

and

$$I_\nu(s) = I_\nu(0) e^{\kappa_{0\nu} s} + \frac{\epsilon_\nu}{\kappa_{0\nu}} (\epsilon^{\kappa_{0\nu} s} - 1) \quad . \tag{3.17}$$

The radiation propagates through the masing medium and the intensity increases exponentially and when a change in the pumping mechanism occurs the maser reacts also exponentially. From Eq. 3.14 and 3.15 we see indeed that the absorption coefficient $\kappa_{0\nu} \propto \Delta N_0$, which means that unsaturated masers may show unpredictable and irregular variability.
When the amplification process produces $J_\nu \gg J_s$, the pumping mechanism has an efficiency $\eta \sim 1$ and the maser reaches the *saturated* regime: the population difference ΔN_ν will crucially decrease, since the stimulated emission drains the upper energy level of the masing cloud.
Considering $J_\nu = I_\nu \Omega / 4\pi$ and $\Omega \simeq \pi r^2 / s^2$, the absorption coefficient under the saturated regime is

$$\kappa_\nu \simeq -\kappa_{0\nu} \frac{J_s}{J_\nu} = -\kappa_{0\nu} J_s \frac{4\pi}{I_\nu \Omega} \simeq -\kappa_{0\nu} J_s \frac{4s^2}{I_\nu r^2} \quad , \tag{3.18}$$

and the resulting radiative transfer equation gives

$$\frac{dI_\nu}{ds} = \kappa_{0\nu} J_s + \frac{4s^2}{r^2} + \epsilon_\nu \quad , \tag{3.19}$$

and integrating between the path lengths s' and s''

$$I_\nu(s'') = I_\nu(s') + \frac{4}{3} \kappa_{0\nu} J_s \left(\frac{s''^3 - s'^3}{r^2}\right) + \epsilon_\nu (s'' - s') \quad . \tag{3.20}$$

While in the unsaturated regime the beaming angle $\Delta\Omega$ is proportional to the inverse of the optical depth, in the saturated case $\Delta\Omega$ is proportional to the inverse of the square of the optical depth. A schematic example of maser beaming is illustrated in Fig. 3.3. The amplification terminates once the maser pass as from the unsaturated to the saturated regime.
The strong amplification in the unsaturated regime reduces the line width of the maser during the propagation of the emission, generating a narrowing effect. Considering a Doppler absorption profile

$$\phi_D(\nu) = \frac{1}{\sqrt{\pi} \Delta\nu_D} e^{-\frac{(\nu - \nu_0)^2}{\Delta\nu_D^2}} \quad , \tag{3.21}$$

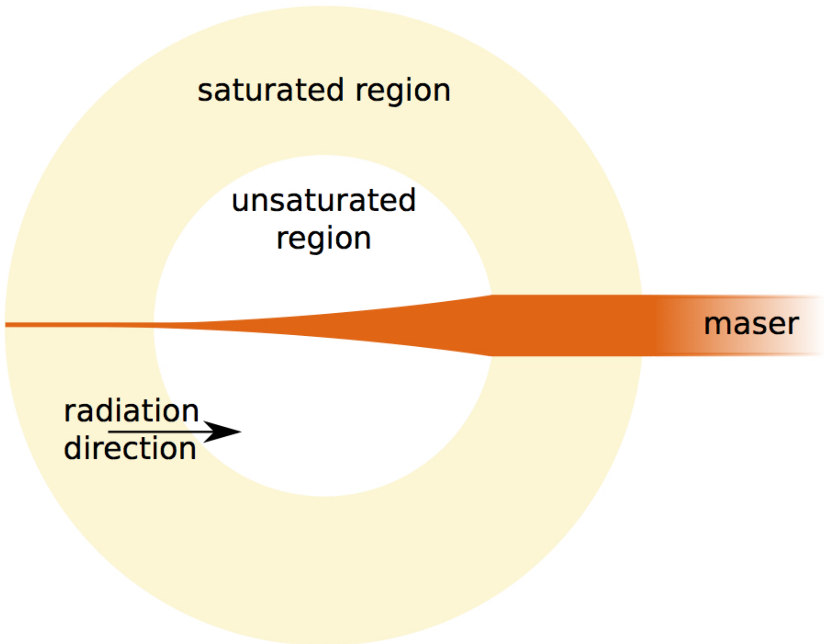

Figure 3.3: Schematic representation of the maser beaming (see Chap. 3.1). The width of the orange beam is proportional to the intensity of the maser; the linear increase in the saturated region is not drawn. The amplification terminates once the maser passes from the unsaturated to the saturated regime.

where ν_0 is the line centre frequency, $\Delta\nu_D = \frac{\nu_0}{c}\sqrt{\frac{2kT}{m}}$, c is the speed of light, T is the temperature of the medium and m is the mass of the molecule.
Given $\kappa_0' = \kappa_0/(\sqrt{\pi}\Delta\nu_D)$, the maser absorption coefficient becomes

$$\kappa_{0\nu} = \kappa_0\phi(\nu) = \kappa_0' e^{-\frac{(\nu-\nu_0)^2}{\Delta\nu_D^2}} \quad , \tag{3.22}$$

from which we can obtain the line narrowing as a function of the path length

$$\nu - \nu_0 = \Delta\nu_D \frac{1}{\sqrt{\kappa_0' s'}} \quad . \tag{3.23}$$

However, the narrowing process cannot continue indefinitely and the line width can reduce only by a finite amount until the central part starts to saturate. This happens while the wings of the line are still growing exponentially, causing a re-broadening of the line. Eventually when the maser is fully saturated $\nu - \nu_0 = \Delta\nu_D$. Eq. (3.20) rules the intensity in the saturated case and the amplification increases linearly along the maser path.

3.2 Polarization

Through the study of linearly and circularly polarized maser emission, it is possible to obtain information about the magnetic field B, such as the strength and direction, at the small scale of circumstellar discs ($\sim 100 - 1000$ au). Masers present narrow and bright spectral lines ideal to detect the Zeeman effect and to measure the Faraday rotation. The first effect happens when, under the action of a magnetic field, the spectral lines of a molecule are separated in several components due to the magnetic sub-levels. The shift is proportional to the magnetic field strength and it is named Zeeman splitting. Faraday rotation causes a rotation of the polarization plane, which is proportional to the magnetic field component in the direction of the propagation. Measuring the variation in the orientation of the magnetic field it is possible to obtain the morphology of B.
Maser observations can probe the presence of magnetic field in regions where the density is $\geq 10^5$ cm^{-3}. Water masers can be used to trace high density and shocked regions, while OH masers can trace a weaker magnetic field in less dense regions. The class I methanol masers are collisionally excited and are associated with shocked H_2 knots in the molecular outflow, while the class II methanol masers are radiatively pumped by IR emission from warm dust (T$\geq$ 150 K), so they can probe B at higher density $\geq 10^6$ cm^{-3} (T$\leq$ 50 K).
The first full polarization observations of 6.7 GHz methanol masers were made by Ellingsen (2002). Thereafter, Green et al. (2007), Vlemmings et al. (2006); Vlemmings (2008); Vlemmings et al. (2010), Dodson & Moriarty (2012) and Surcis et al. (2012, 2014, 2015) established that maser emission (from e.g. methanol and water) are reliable probes to test magnetic fields. However, this has been done only in a limited number of cases which still prevents building a complete picture of the role played by magnetic fields. Most importantly, what is still lacking is more observational evidence that the magnetic field at the small scales probed by masers tracks the field at larger scales, probed e.g. by the dust, and not small-scale fluctuations. Currently only a few cases of both masers and dust polarization were observed towards the same regions (e.g. Surcis et al. 2014).
One of these cases is the high mass protostar IRAS 18089-1732, that is the subject on which I focused in this work.

Chapter 4

The case of IRAS 18089-1732

The high mass protostar IRAS 18089-1732 is especially important because dust emission observations have already revealed the structure of the magnetic field at large scales of $\sim$ 5000 au (Beuther et al. 2010). In the paper presented in this thesis we investigated the small-scale magnetic field of this source. We analysed a three-epoch Multi-Element Radio Linked Interferometer Network (MERLIN) observation of the 6.7 GHz CH_3OH (methanol) maser generated in the same region of the disc, where dust was already observed. When we refer to "large" scales, we indicate scales within a $\sim 4''$ region (about 9000 au), centred on IRAS 18089-1732, and to "small" scales for size of a typical maser region $\sim$ 10 mas (about 20 au).
IRAS 18089-1732 (hereafter IRAS 18089) is a protostar located at a distance of 2.34 kpc (Xu et al. 2011) and with a velocity v_{lsr}=33.8 km s^{-1} (Beuther et al. 2005). The luminosity is $L = 1.3 \sim 10^4\ L_\odot$ (evaluated by Sridharan et al. 2002 and also rescaled to the adopted distance), and the mass of the gas is $M \sim 1000\ M_\odot$ (estimate from single dish millimetre continuum observations by Beuther et al. 2002 and rescaled to the adopted distance).
IRAS 18089 is a hot core (see Sec. 2.3.2 and Fig. 2.5) and presents its typical chemistry and line forest profile with strong molecular emission, coming from e.g. $HCOOCH_3$, H_2S, SO, and SO_2, as shown in Fig. 4.1.
The source presents also a disc-outflow system. The Submillimiter Array (SMA) observed a SiO(5-4) molecular outflow elongated in about the north-south direction and several molecular lines presented the rotational signatures typical of an accreting disc in the dense gas perpendicular to the outflow. A possible representation of this scenario compared with previous observations is illustrated in Fig. 4.2.
A linear polarization fraction up to 8% was detected for the CO(3-2), trough the Goldreich-Kylafis effect. The resulting magnetic field structure is largely aligned with the jet-outflow orientation, from the smaller scales of the core to the larger scales of the outflow. Beuther et al. (2010) estimated magnetic field strength in

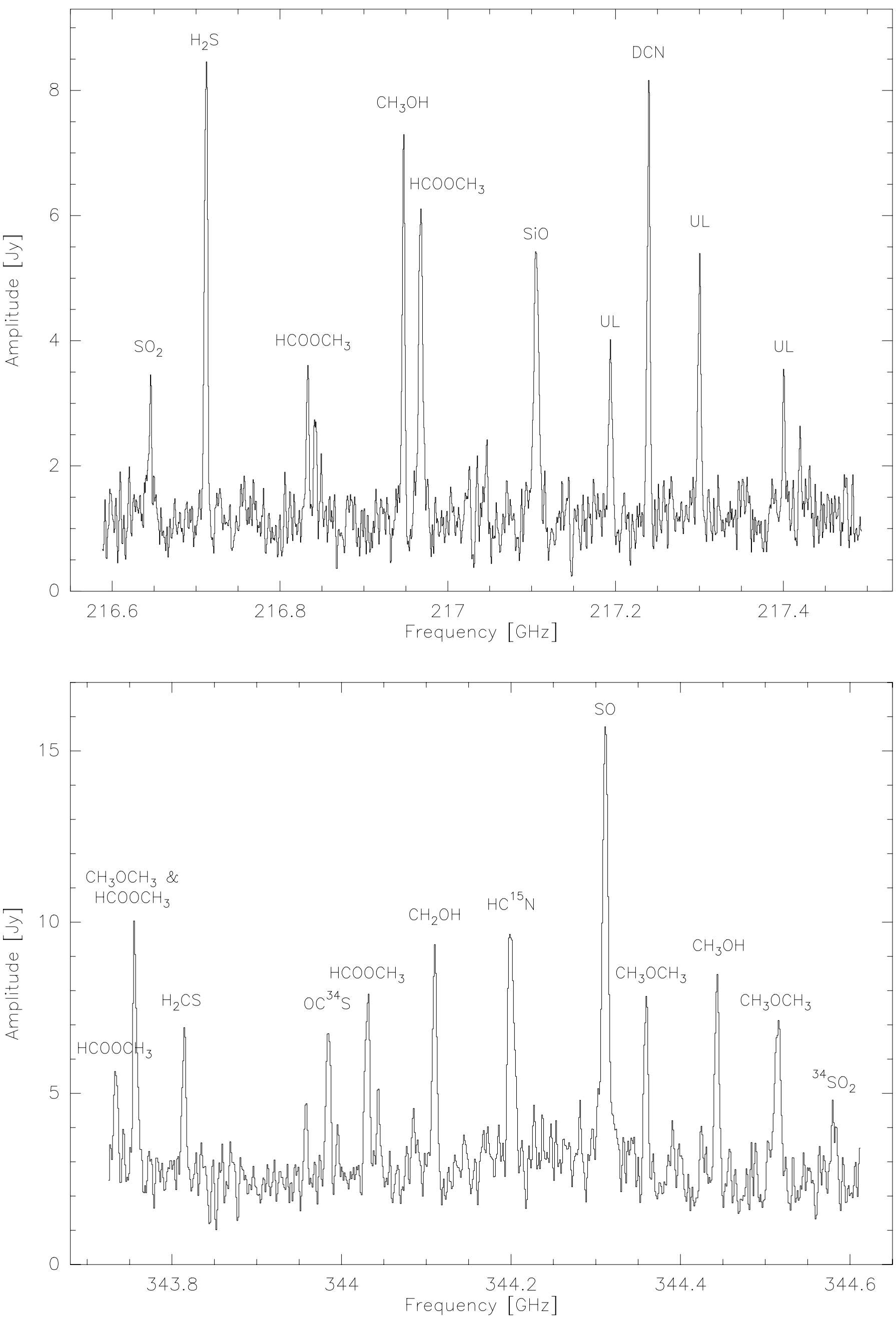

Figure 4.1: SMA spectra toward the high-mass star-forming region IRAS 18089-1732 (Beuther et al. 2004). UL marks unidentified lines. The spectra show the typical chemistry of an hot core (see Sec. 2.3.2 and Fig. 2.5).

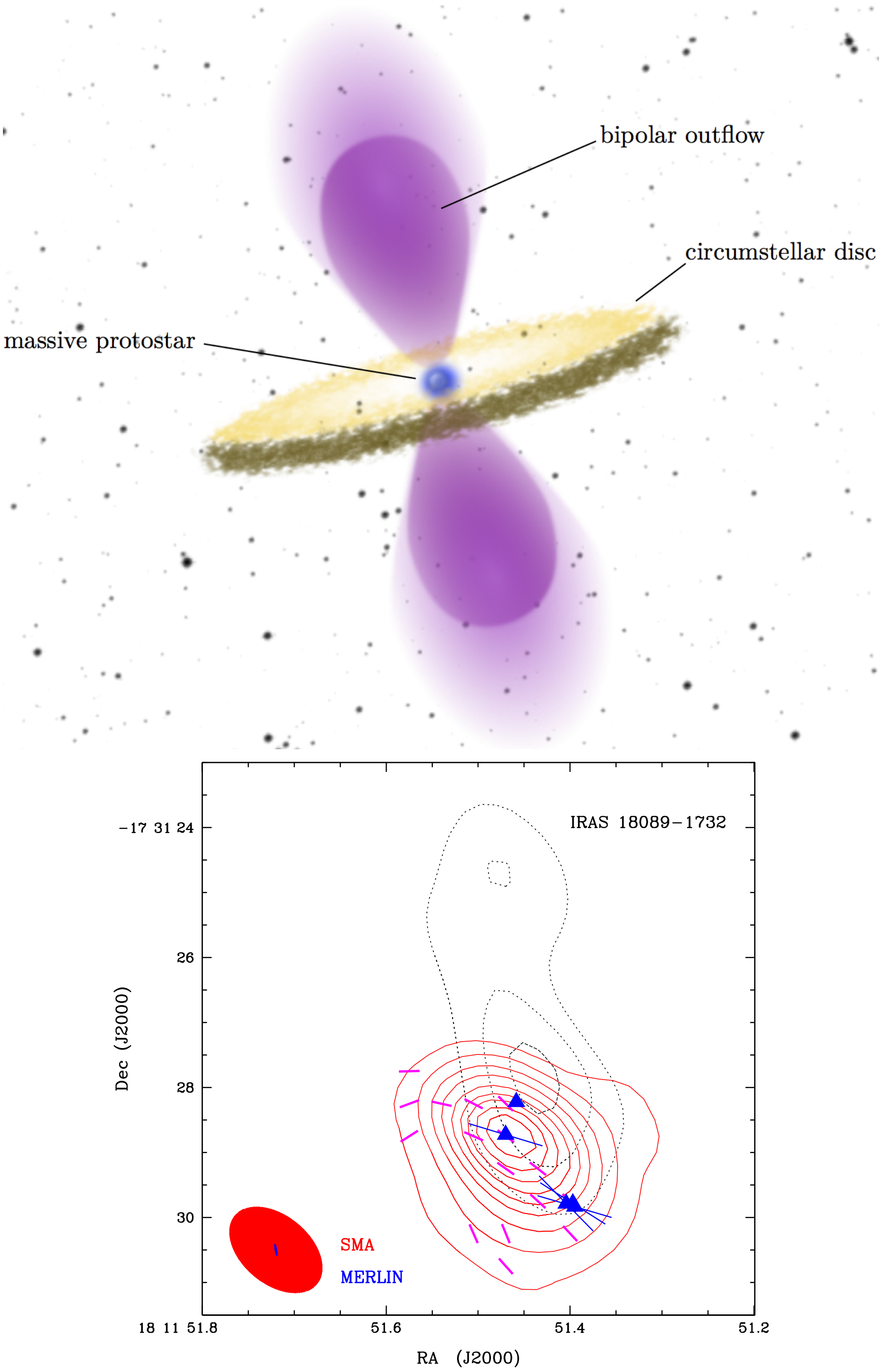

Figure 4.2: **Top panel**: a cartoon of the morphology of IRAS 18089-1732, illustrating bipolar outflows and the accreting disc. **Bottom panel**: the red contours show the integrated Stokes I image of the continuum emission in 10σ steps. Dotted black contours show the SiO(5-4) emission, tracing the outflow, integrated from 30 to 40 km s^{-1} (5σ steps of 260 mJy beam^{-1}). The magenta line segments plot the orientation of the magnetic field derived from dust polarization (obtained with SMA, Beuther et al. 2010). The blue triangles mark the position of methanol masers and the blue lines indicate the direction of the magnetic field from methanol maser linear polarization (MERLIN observations discussed in this work).

the plane of the sky of $B_{pos} \sim 11$ mG at a core density of 5×10^7 cm^{-3}. This value was obtained from SMA observation of dust continuum emission at 880 μm.
Vlemmings (2008) derived a similar line-of-sight magnetic field strength $B_{los} \sim 8$ mG from the Zeeman splitting of the 6.7 GHz CH_3OH maser line, at densities higher than 10^6 cm^{-3}. However this evaluation was made using an extrapolation of the g-factor, obtained from measurements of 25 GHz methanol transitions. This may lead to a derived magnetic field strength that is larger by an order of magnitude with respect to the true field strength, as described by Vlemmings et al. (2011).
The total magnetic field strength was $B_{tot} \sim \sqrt{B_{pos}^2 + B_{los}^2} \sim 14$ mG, of the same order of measurements made by Girart et al. (2009), Surcis et al. (2009), and Vlemmings et al. (2010) for similar sources.
From Australia Telescope Compact Array (ATCA) observations, Walsh et al. (1998) provided a map of IRAS 18089 masers and obtained relative and absolute positions with an accuracy of around $0.05''$ and $1''$ respectively. Goedhart et al. (2009), monitoring the variability in IRAS 18089, reported a periodicity of the flares maxima of around 29.5 ± 0.1 days, derived after 9 years of observations with the Hartebeesthoek Radio Astronomy Observatory 26 m telescope.

Chapter 5

MERLIN observations and data reduction

5.1 Observations

5.1.1 MERLIN

The Multi-Element Radio Linked Interferometer Network (MERLIN), is an array of seven radio telescopes distributed across the UK, with a maximum baseline of 217 km (see 5.1). The antennas are connected to a central correlator located at the Jodrell Bank Observatory (JBO) and operated as a radio-interferometer. The array has been recently upgraded becoming e-MERLIN. The paper discussed in this thesis makes use of data coming from MERLIN.

5.1.2 Observation details

MERLIN observed IRAS 18089-1732 at 6.7 GHz, in March, April, and July 2008. The March and July observations consisted of a single run each, while two runs were performed in April, over two consecutive days. The observations were made using a single spectral window, covering a bandwidth of 249 kHz on March and April, and a bandwidth of 498 kHz in July. The spectral window included 255 channels, reaching a spectral resolution of ~ 0.04 km s^{-1} in March and April, and ~ 0.09 km s^{-1} in July. The total observing time on-source was 28 hours and the data were stored into three datasets. For the first two observations six antennas were used (Lovell was excluded), and for the last observation five antennas (Defford was also not included). In Table 5.1 the observational details are presented.

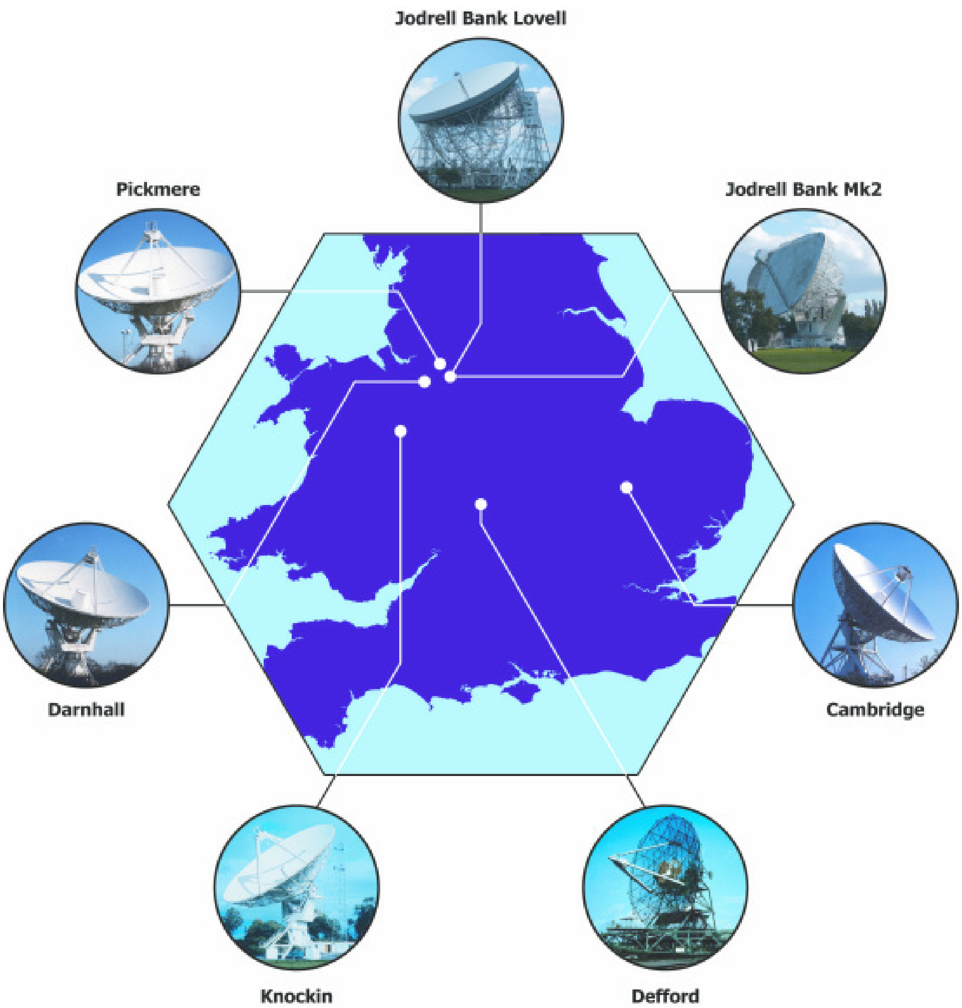

Figure 5.1: The MERLIN array (Credits: MERLIN/VLBI National Facility).

5.2 Data reduction

5.2.1 Data reduction philosophy

Interferometric data reduction is not an easy task. Different factors (e.g. instrument and atmosphere) can act together and corrupt the astronomical signal. Thus it is important to disentangle them, to correct for such effects and to make the visibilities as close as possible to the ideal ones. Several steps are involved in the data reduction process: editing of data, also known as flagging, calibration of flux, amplitude, phase and polarization, imaging and analysis. In the data editing phase, we essentially decide what data to discard and we must find the best trade-off between retaining the maximum information and improving the cleanliness of data. Therefore it is important to understand the reasons for flagging (or not flagging)

Table 5.1: Observational details for IRAS 18089-1732.

Observation date	Polarization mode	Channel spacing (km s^{-1})	Bandwidth$^{(a)}$ (kHz)	Beam size (arcsec × arcsec)	Position Angle (∘)	RMS$^{(b)}$ (Jy beam^{-1})
13 March 2008	RR, LL, RL, LR	∼0.05	249	0.18 × 0.03	10.11	0.03
7–8 April 2008	RR, LL, RL, LR	∼0.05	249	0.18 × 0.03	12.39	0.02
4 July 2008	RR, LL	∼0.09	498	0.24 × 0.08	-16.34	0.04

(a) The spectral window included 255 channels.
(b) RMS on the line free channels.

any data, since there is no unique flagging recipe, and checks have to be done case by case. While the data inspection and flagging concerns spurious amplitude and phase fluctuations due to instrumental problems, the calibration consists firstly in estimating the amplitude and phase variations in time and frequency that can be measured and corrected for. Moreover, in order to calibrate polarization it is necessary to correct for the instrumental leakage terms, calibrate the delay between R and L polarization and to set the absolute polarization position angle.
The different steps of data calibration should not be "sealed off" from each other. It means that if something wrong were discovered after calibration, we would need to return on our steps to better check the data. Once the visibilities are calibrated, we have measured a sample of the Fourier Transform of the sky brightness from which we can build an image. This process is also problematic because the incomplete sampling of the uv-plane results after the Fourier transform in a dirty map, which is the convolution of the brightness distribution by the dirty beam. To get a more useful image, one needs to clean this dirty map, using a deconvolution process and setting the input parameters which would allow to get the best results (clean algorithm, weighting, etc.).

5.2.2 Data inspection and flagging

The data reduction was carried out using the Astronomical Image Processing Software (AIPS version DEC 2016) and building a *ParselTongue* pipeline which was applied to all the three epochs (ParselTongue is a Python interface to AIPS). We inspected and edited the data, by using the AIPS visibility plotting tasks (e.g. *uvplot, vplot*) and the flagging task *uvflag*, paying particular attention to any excursion in amplitude or phase depending on time and/or frequency, mostly due to instrumental errors. We also removed bad channels and those at the edges of the spectral window. We selected MK2 as "reference antenna" that was used in all the calibration steps. An interferometer measures phase differences, thus there is no absolute phase reference. The phase of the reference antenna is fixed to zero and the phases of all the other antennas are taken as relative to the reference one. It is customary to select an antenna that is known to be particularly stable, as any gain jumps will be transferred to the other antenna solutions. Also, it is best to choose a reference antenna that never drops out during the observations.

5.2.3 Calibration

The calibration process is based on four important steps (the name of the related AIPS task are reported in parenthesis):

- the calibration of the frequency response of the instrument, also known as bandpass calibration. This step corrects for gain variations at different frequencies, mostly due to instrumental effects (*bpass*);
- the calibration of the phase and amplitude, which corrects for the phase and amplitude variation due to instrumental or atmospheric causes (*calib* and *clcal*);
- the calibration of the flux, which allows to obtain absolute fluxes from the measured amplitudes, by scaling them on the basis of observations of a calibrator object, whose flux is already known (*setjy* and *getjy*);
- the calibration of polarization which gives the correct polarized flux removing the polarization residuals given by the instrumentation (*pcal*) and sets the absolute polarization position angle by correcting the systematic delay between R and L polarization (*clcor*).

The quasar 3C84 was used to calibrate bandpass, amplitude and polarization leakages, MRC 1757-150 was the phase calibrator and 3C286 was chosen as the flux and polarization angle calibrator. For the flux calibration we used a model of 3C286 provided by the MERLIN staff[1], since 3C286 it is known to be resolved at the observed frequency of 6.7 GHz.
In order to check the quality of the calibration we first applied the calibration table to the phase-calibrator and then to the target.
Unfortunately in the second run of April the phase calibration failed, since no phase-calibrator was observed in that timerange: so we assumed a model produced on strongest maser of the first run to self calibrate the second run. In Table 5.3 we report the fluxes of each calibrator. The LRS correction was applied to ensure constant velocity in the target frame.
We performed a self-calibration on the brightest maser feature of each epoch, whose peak flux density was $\sim$ 70 Jy beam^{-1} in March, $\sim$ 122 Jy beam^{-1} in April and $\sim$ 75 Jy beam^{-1} in July; in each case the velocity was V_{lsr}=39.2 km s^{-1}. Since IRAS 18089 was observed in full polarization mode during March and April, while the July epoch had dual circular polarization only (see Table 5.1), the linear polarization calibration was performed uniquely for the first two epochs. To compute

[1] http://www.e-merlin.ac.uk/data-red/

Table 5.3: Fluxes [Jy] of the calibrators used in the three epochs.

Observation date	3C84 (observed)	MRC 1757-150 (observed)	3C286 (model)
13 March 2008	10.32	0.14	5.70
7–8 April 2008	14.26	0.14	5.70
4 July 2008	15.14	0.15	5.70

the instrumental polarization (aka D-terms or antenna leakage), we used 3C84 which is a zero polarization calibrator. The leakages were then applied to the antenna tables of all the calibrators. We estimated the R-L phase difference using 3C286, which is a standard well-known polarized calibrator with a stable polarization angle of 33.0° at 6.7 GHz. The delay between the R and L polarizations is twice the source polarization angle. The angle correction was applied first to 3C286 and then copied to the target.

5.2.4 Imaging

Using the AIPS task *imagr* we extracted one image in the Stoke I, at low resolution $0.012''$ and big size $12'' \times 12''$ in order to look for maser emission inside a wide field. Then we cleaned the I, Q, U, and V cubes with an image size of $6.14'' \times 6.14''$ and a cell size of $0.006''$. In Fig. 5.2 we plot the spectra of the three epochs, obtained by summing all the pixels in the Stoke I image for each channel.
The RMS noise in the line-free channels is given in Table 5.1; however, since the noise is dominated by the dynamic range limitations, the noise increases in the channels with strongest maser features. In March, the noise increased up to $\sim$0.2 Jy beam^{-1} in I, $\sim$0.17 Jy beam^{-1} in Q, $\sim$0.13 Jy beam^{-1}in U and $\sim$0.05 Jy beam^{-1} in V. In April, the noise reached $\sim$0.2 Jy beam^{-1} in I, $\sim$0.25 Jy beam^{-1} in Q, $\sim$0.15 Jy beam^{-1} in U and $\sim$0.07 Jy beam^{-1} in V. In July we only have maps in Stokes I and V, and in the channels with the strongest features, the noise increased up to $\sim$0.12 Jy beam^{-1} and $\sim$0.06 Jy beam^{-1}, respectively.
The estimated residual leakages in all epochs are less than the RMS noise.
The U and Q datacubes are combined to produce cubes of polarized intensity (POLI=$\sqrt{Q^2 + U^2}$) and polarization angle (POLA $= 1/2 \times \mathrm{atan}(U/Q)$). The error on POLA takes into account the formal error due to the thermal noise (Wardle & Kronberg 1974), which is $\sigma_{POLA} = 0.5(\sigma_P/POLI) \times (180°/\pi)$, where σ_P is the RMS of POLI. We compared the linear polarization angles for 3C286 measured in our observations with the angles reported by the NRAO in the Polarization Calibration Database[2]. After the calibration, we found angles of $38° \pm 5°$ and $36° \pm 3°$ in March and April respectively, which are consistent with the angle given in the database.

[2]www.vla.nrao.edu/astro/calib/polar/2008

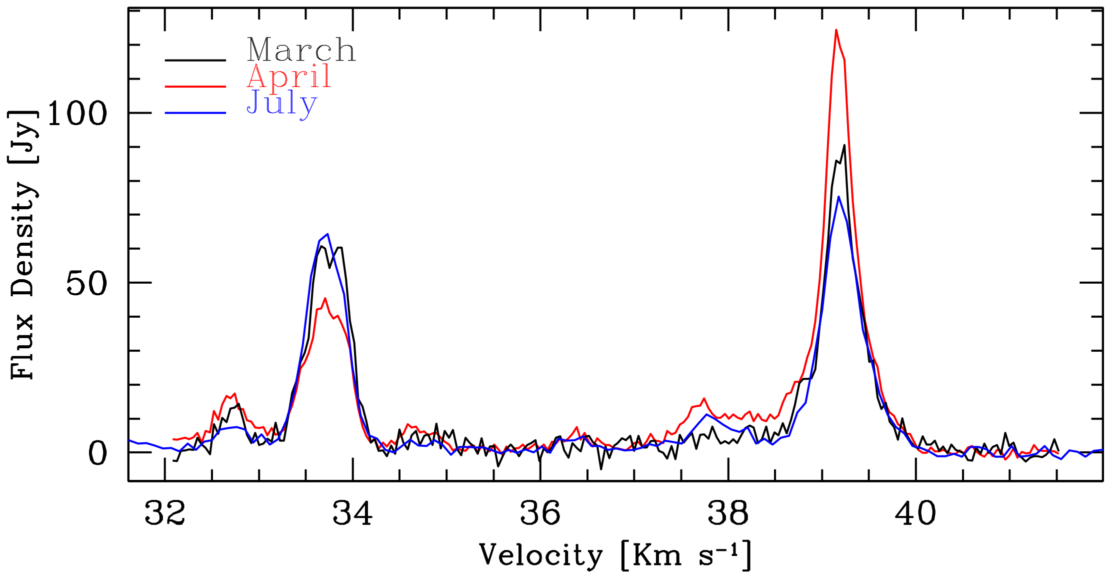

Figure 5.2: 6.7 GHz methanol maser spectra of the three epochs, obtained by summing all the pixel in the image for each channel.

We adopted the same maser identification method already reported in Surcis et al. (2011). We used the code called *maser finder* which search for maser features, inspecting the datacube velocity channel by velocity channel. The code identify a maser spot if its signal to noise ratio is greater than a predefined value (for our data we chose 8 and we considered the local rms). Making use of the AIPS task *imfit*, we performed a Gaussian fit for each feature and we generate a table including maser parameters, such as velocities, positions and peak flux densities. We consider a maser feature as identified, only when the maser spots appear in at least three consecutive velocity channel and present the same position.

Chapter 6

Introduction to Paper I

By analysing the MERLIN Dataset we identified 9 masers in March and April and 7 masers in July, confirming almost all the maser features already seen in previous works (see Chap. 4) and presenting some new detections. In Table 6.1 I report all the maser features observed in March and plotted in Fig. 6.1 (for the April and July detections see the attached paper). The average position of F.01 in the three epochs is $\alpha_{2000} = 18^{\mathrm{h}}11^{\mathrm{m}}51.398^{\mathrm{s}} \pm 0.002^{\mathrm{s}}$, $\delta_{2000} = -17^{\circ}31'29.92'' \pm 0.02''$. In March, the offset of F.01 from its average position is -33 mas in RA and 4.3 mas in Dec. July observations were in dual circular polarization only, so the linear polarization analysis was performed only on the masers observed in the first two epochs, for which we measured the median linear polarization fraction (P_l) and the median linear polarization angle (χ) across the spectrum. We identified two groups of masers on the basis of two different velocities and χ values: a blue group spanning a velocity range from 30.0 to 36.4 km s^{-1}, and a red group from 37.7 to 39.2 km s^{-1}.

The two groups of masers showed ordered linear polarization vectors, and the orientation was preserved in both March and April observations. The blue group had a weighted average angle of $\chi_{B,M} = -24^{\circ} \pm 8^{\circ}$ in March and $\chi_{B,A} = -31^{\circ} \pm 12^{\circ}$ in April. The red group had only one linearly polarized emission in March with an angle $\chi_{R,M} = -78^{\circ} \pm 5^{\circ}$, while in April the weighted polarization angle was $\chi_{R,A} = -70^{\circ} \pm 2^{\circ}$.

The brightest features were expected to be close to maxima in all three epochs on the basis of the variability analysis by Goedhart et al. (2009), but for two of the epochs they showed a flux density much lower than predicted by previous works, suggesting a change in magnitude or irregular periodicity or both. Our positions, more accurate compared with previous measures, confirmed the separations of features, and suggested lower limits to light travel time, that are in some cases incongruous with the simplest interpretations of time delays.

From the monitoring by Goedhart et al. (2009), we noticed that all the masers

Table 6.1: Parameters of the 6.7-GHz methanol maser features detected in IRAS 18089-1732 in March.

(1) Maser	(2) RA^a offset (mas)	(3) Dec^a offset (mas)	(4) Peak flux Density(I) (Jy beam^{-1})	(5) $V_{\rm lsr}$ (km s^{-1})	(6) P_l^b (%)	(7) χ^b ($\circ$)	(8) ΔV_L (km s^{-1})	(9) P_V (%)	(10) B_{los} (mG)
F.01	0	0	69.99 ± 0.66	39.24	8.9 ± 1.4	-78 ± 5	–	–	–
F.02	-34.90	14.11	8.53 ± 0.13	38.84	–	–	–	–	–
F.03	43.68	-2.46	5.19 ± 0.06	37.75	–		–	–	–
F.04	28.92	15.60	3.23 ± 0.04	36.43	–	–	–	–	–
F.05	157.26	51.95	4.12 ± 0.05	34.67	–	–	–	–	–
F.06	1098.47	1128.63	40.04 ± 0.40	33.84	3.8 ± 2.7	-50 ± 28	0.4	0.8	5.5 ± 1.7
F.07	54.65	54.52	17.10 ± 0.27	33.53	6.3 ± 0.4	-31 ± 1	–	–	–
F.08	55.04	44.99	6.45 ± 0.07	32.74	9.4 ± 0.3	-16 ± 1	–	–	–
F.09	937.80	1620.90	3.45 ± 0.07	32.70	–	–	–	–	–

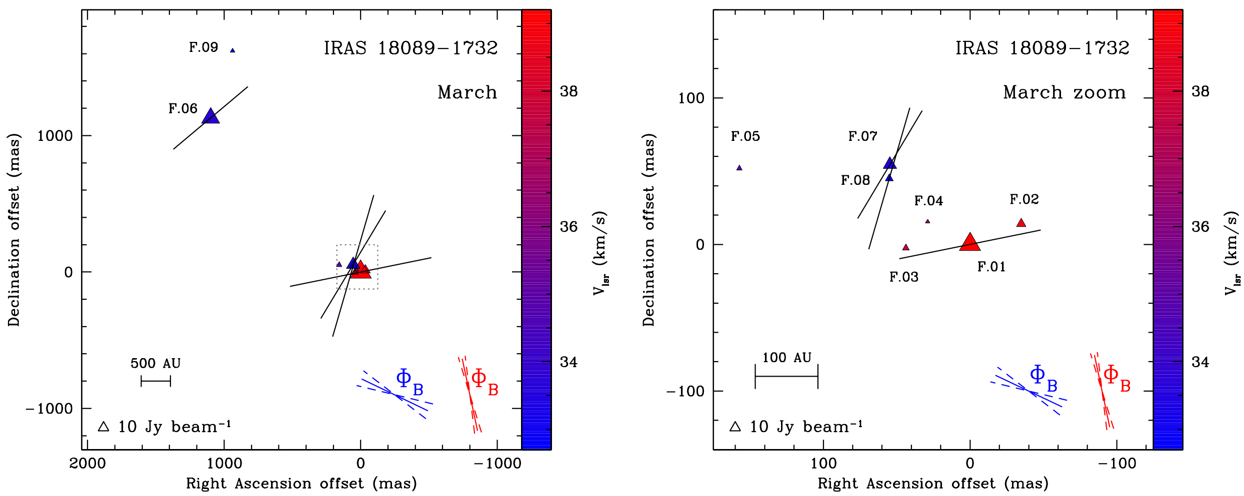

Figure 6.1: Masers identified in March as listed in Table 6.1. The right panel shows a zoom of the region marked by the dashed grey boxes in the left panel. Each maser is represented by a triangle. The different sizes of the triangles represent the intensity, while the colours indicate the velocity of the maser feature, according to the scale reported in the colour bar. Line segments mark the direction of the polarization angle for the maser features that show linear polarization. The average direction of the resulting magnetic field Φ_B obtained for the blue and red groups of masers is indicated in the bottom right corners of each panel.

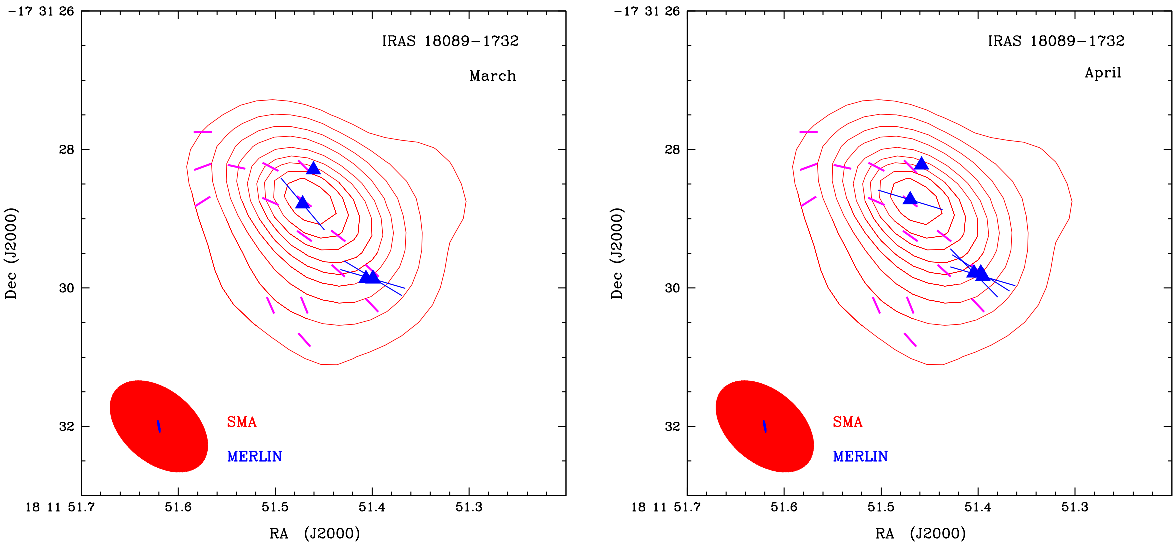

Figure 6.2: Masers in the blue group (blue triangles and blue segments) superimposed on the integrated I image of the dust continuum emission observed by Beuther et al. (2010) at 880 μm with SMA (red contours; the contours are drawn in 10σ steps). The magenta line segments show the magnetic field orientation obtained by linearly polarized dust emission (Beuther et al. 2010). The blue segments represent the magnetic field orientation obtained by our linearly polarized methanol maser emission; it is consistent in March (left panel) and April (right panel) therefore the magnetic field follows the same direction indicated by the dust emission. The red and blue ellipses show the beams of SMA ($1.65'' \times 1.05''$, position angle $51°$) and MERLIN, respectively.

in the red group showed variability, with peaks occurring ahead of that of the reference feature, while those in the blue group lag behind. Therefore, since the two groups are separated in polarization angles and velocities, we concluded that the two groups of masers are generated in two different zones, one located on the base of the molecular outflow and another one laying on the disc of the protostar. Consequently, we suggest they are probing two different magnetic field directions, and the resulting orientation on the plane of the sky of $\Phi^{disc} = +62° \pm 3°$ and $\Phi^{outflow} = +14° \pm 4°$.
We showed that the small-scale magnetic field probed by the masers is consistent with the large-scale magnetic field traced by the dust (see Fig. 6.2 where we overplotted polarized dust emission from Beuther et al. 2010 and my results).
Therefore we conclude that the large scale field component (traced by dust), prevails over any small scale field fluctuations (traced by masers).
For one of the brightest features, we proposed a tentative detection of circular polarization. Between March and April, the spectral profiles of the total power and of the circular polarization appear to invert. We presented three possible explana-

tions. The reversal could be caused by the splitting of two hyperfine components, each one emitting preferentially in a different epoch. The second possibility could be that the magnetic field inverted its sign. Finally it could be attributable to two different masers, originated in two distinct places but lying along the same line of sight. For all the options, we obtained a $|B_{los}| \sim 5$ mG, comparable to $B_{pos} \sim 11$ mG already obtained by Beuther et al. (2010) for dust.

6.1 Future prospects

New insights on the topic discussed in this thesis might come from increasing the number of cases in which line polarization is observed. For example, one could aim at detecting the Goldreich-Kylafis effect in more cases, by inspecting for example the thermal molecular emission coming from the different shells of hot cores. Analyzing polarized spectra we could obtain information about the strength and the morphology of the magnetic field coming from various environments and tracing different densities and optical depths. Comparing the results with the data already obtained from polarized dust observations and methanol masers, we will be able to derive a 3D structure of the magnetic field.
Interferometers such ALMA can provide enough sensitivity to enable this kind of study. The High Mass Star Formation Legacy Project is currently ongoing with the updated eMERLIN. The project is observing young stellar objects in several evolutionary stages providing a new panorama on the evolutionary stages of massive protostars. The goal is to clarify the physical mechanisms involved in the formation process, such as the ones involved in the creation of jets and outflows.

Useful reviews and books

Finally, in this Chapter I present a list of useful books and comprehensive reviews which I made use of in this work.

Beuther, H., Klessen, R., Dullemond, C., & Henning, T. 2014, Protostars and Planets VI, Space Science Series (University of Arizona Press)

Beuther, H., LInz, H., Henning, T., & of the Pacific, A. S. 2008, Massive Star Formation: Observations Confront Theory : Proceedings of a Conference Held at the Heidelberg Convention Center, Heidelberg, Germany, 10-14 September 2007, Astronomical Society of the Pacific conference series (Astronomical Society of the Pacific)

Bodenheimer, P. 2011, Principles of Star Formation, Astronomy and Astrophysics Library (Springer Berlin Heidelberg)

Bonnell, I. A. & Smith, R. J. 2011, in IAU Symposium, Vol. 270, Computational Star Formation, ed. J. Alves, B. G. Elmegreen, J. M. Girart, & V. Trimble, 57

Braithwaite, J. 2012, MNRAS, 422, 619

Chabrier, G. 2005, in Astrophysics and Space Science Library, Vol. 327, The Initial Mass Function 50 Years Later, ed. E. Corbelli, F. Palla, & H. Zinnecker, 41

Cortes, P. C., Crutcher, R. M., & Watson, W. D. 2005, ApJ, 628, 780

Draine, B. T. 2011, Physics of the Interstellar and Intergalactic Medium (Princeton University Press)

Elitzur, M. 2002, in Astrophysical Spectropolarimetry, ed. J. Trujillo-Bueno, F. Moreno-Insertis, & F. Sánchez, 225–264

Elitzur, M. 2012, Astronomical Masers, Astrophysics and Space Science Library (Springer Netherlands)

Gray, M. 2012, Maser Sources in Astrophysics (Cambridge University Press)

Krumholz, M. R. 2011, in American Institute of Physics Conference Series, Vol. 1386, American Institute of Physics Conference Series, ed. E. Telles, R. Dupke, & D. Lazzaro, 9–57

Krumholz, M. R., Bate, M. R., Arce, H. G., et al. 2014, Protostars and Planets VI, 243

LeBlanc, F. 2010, An Introduction to Stellar Astrophysics (Wiley)

McKee, C. F. & Tan, J. C. 2003, ApJ, 585, 850

Nedoluha, G. E. & Watson, W. D. 1992, ApJ, 384, 185

Reipurth, B. & Schneider, N. 2008, Star Formation and Young Clusters in Cygnus, ed. B. Reipurth, 36

Schulz, N. 2005, From Dust To Stars: Studies of the Formation and Early Evolution of Stars, Springer Praxis Books (Springer Berlin Heidelberg)

Surcis, G., High resolution magnetic field measurements in high-mass star-forming regions, PhD Thesis, University of Bonn, 2011

Tan, J. C., Beltrán, M. T., Caselli, P., et al. 2014, Protostars and Planets VI, 149

Troland, T. H. & Heiles, C. 1982, ApJ, 252, 179

Vlemmings, W. H. T., Circumstellar maser properties through VLBI observations, PhD Thesis, Leiden University, 2002.

Ward-Thompson, D. & Whitworth, A. 2011, An Introduction to Star Formation (Cambridge University Press)

Bibliography

André, P. 2002, in EAS Publications Series, Vol. 3, EAS Publications Series, ed. J. Bouvier & J.-P. Zahn, 1–38

André, P., Ward-Thompson, D., & Barsony, M. 1993, ApJ, 406, 122

Arce, H. G., Shepherd, D., Gueth, F., et al. 2007, Protostars and Planets V, 245

Awad, Z., Viti, S., Collings, M. P., & Williams, D. A. 2010, MNRAS, 407, 2511

Beltran, M. 2011, Lecture at the International Training School "Astrochemistry with ALMA"; www.alma.inaf.it/attachments/article/118/Lecture10-Beltran.pdf

Beltrán, M. T. & de Wit, W. J. 2016, A&A Rev., 24, 6

Beuther, H., Hunter, T. R., Zhang, Q., et al. 2004, ApJ, 616, L23

Beuther, H., Schilke, P., Menten, K. M., et al. 2002, ApJ, 566, 945

Beuther, H., Vlemmings, W. H. T., Rao, R., & van der Tak, F. F. S. 2010, ApJ, 724, L113

Beuther, H., Zhang, Q., Sridharan, T. K., & Chen, Y. 2005, ApJ, 628, 800

Bonnell, I. A. & Bate, M. R. 2006, MNRAS, 370, 488

Brand, J., Massi, F., Zavagno, A., Deharveng, L., & Lefloch, B. 2011, A&A, 527, A62

Crutcher, R. M., Wandelt, B., Heiles, C., Falgarone, E., & Troland, T. H. 2010, ApJ, 725, 466

Dodson, R. & Moriarty, C. D. 2012, MNRAS, 421, 2395

Duquennoy, A. & Mayor, M. 1991, A&A, 248, 485

Ellingsen, S. P. 2002, in IAU Symposium, Vol. 206, Cosmic Masers: From Proto-Stars to Black Holes, ed. V. Migenes & M. J. Reid, 151

Girart, J. M., Beltrán, M. T., Zhang, Q., Rao, R., & Estalella, R. 2009, Science, 324, 1408

Girart, J. M., Rao, R., & Marrone, D. P. 2006, Science, 313, 812

Goedhart, S., Langa, M. C., Gaylard, M. J., & van der Walt, D. J. 2009, MNRAS, 398, 995

Gonçalves, J., Galli, D., & Girart, J. M. 2008, A&A, 490, L39

Gould, R. J. & Salpeter, E. E. 1963, ApJ, 138, 393

Green, J. A., Richards, A. M. S., Vlemmings, W. H. T., Diamond, P., & Cohen, R. J. 2007, MNRAS, 382, 770

Healy, K. R., Hester, J. J., & Claussen, M. J. 2004, ApJ, 610, 835

Hester, J. J. & Desch, S. J. 2005, in Astronomical Society of the Pacific Conference Series, Vol. 341, Chondrites and the Protoplanetary Disk, ed. A. N. Krot, E. R. D. Scott, & B. Reipurth, 107

Hollenbach, D. & Salpeter, E. E. 1971, ApJ, 163, 155

Karr, J. L. & Martin, P. G. 2003, ApJ, 595, 900

Kouwenhoven, M. B. N., Brown, A. G. A., Goodwin, S. P., Portegies Zwart, S. F., & Kaper, L. 2009, A&A, 493, 979

Krasnopolsky, R. & Gammie, C. F. 2005, ApJ, 635, 1126

Lada, C. J. 1987, in IAU Symposium, Vol. 115, Star Forming Regions, ed. M. Peimbert & J. Jugaku, 1–17

Lefloch, B. & Cernicharo, J. 2000, ApJ, 545, 340

McKee, C. F. & Tan, J. C. 2003, ApJ, 585, 850

Mouschovias, T. C. 1976, ApJ, 206, 753

Mouschovias, T. C. & Spitzer, Jr., L. 1976, ApJ, 210, 326

Pound, M. W. 1998, ApJ, 493, L113

Seifried, D., Banerjee, R., Pudritz, R. E., & Klessen, R. S. 2015, MNRAS, 446, 2776

Shu, F. H., Adams, F. C., & Lizano, S. 1987, ARA&A, 25, 23

Shu, F. H., Galli, D., Lizano, S., & Cai, M. 2006, ApJ, 647, 382

Snyder, L. E., Buhl, D., Zuckerman, B., & Palmer, P. 1969, Physical Review Letters, 22, 679

Sridharan, T. K., Beuther, H., Schilke, P., Menten, K. M., & Wyrowski, F. 2002, ApJ, 566, 931

Surcis, G., Vlemmings, W. H. T., Curiel, S., et al. 2011, A&A, 527, A48

Surcis, G., Vlemmings, W. H. T., Dodson, R., & van Langevelde, H. J. 2009, A&A, 506, 757

Surcis, G., Vlemmings, W. H. T., van Langevelde, H. J., & Hutawarakorn Kramer, B. 2012, A&A, 541, A47

Surcis, G., Vlemmings, W. H. T., van Langevelde, H. J., et al. 2015, A&A, 578, A102

Surcis, G., Vlemmings, W. H. T., van Langevelde, H. J., Moscadelli, L., & Hutawarakorn Kramer, B. 2014, A&A, 563, A30

Tan, J. C., Beltrán, M. T., Caselli, P., et al. 2014, Protostars and Planets VI, 149

Vázquez-Semadeni, E., Kim, J., Shadmehri, M., & Ballesteros-Paredes, J. 2005, ApJ, 618, 344

Vlemmings, W. H. T. 2008, A&A, 484, 773

Vlemmings, W. H. T., Diamond, P. J., van Langevelde, H. J., & Torrelles, J. M. 2006, A&A, 448, 597

Vlemmings, W. H. T., Surcis, G., Torstensson, K. J. E., & van Langevelde, H. J. 2010, MNRAS, 404, 134

Vlemmings, W. H. T., Torres, R. M., & Dodson, R. 2011, A&A, 529, A95

Walsh, A. J., Burton, M. G., Hyland, A. R., & Robinson, G. 1998, MNRAS, 301, 640

Wardle, J. F. C. & Kronberg, P. P. 1974, ApJ, 194, 249

Weaver, H., Williams, D. R. W., Dieter, N. H., & Lum, W. T. 1965, Nature, 208, 29

Xu, Y., Moscadelli, L., Reid, M. J., et al. 2011, ApJ, 733, 25

Zavagno, A., Deharveng, L., Comerón, F., et al. 2006, A&A, 446, 171

Zinnecker, H. & Yorke, H. W. 2007, ARA&A, 45, 481

Acknowledgements

First of all, I want to deeply thanks my supervisor Prof. Wouter Vlemmings for introducing me to the fascinating field of massive star formation and masers. Thank you for giving me the freedom to organize myself, my studies and my work and for the patience demonstrated in tutoring me during these years. Thank you also for all your precious suggestions, the precise comments and for the prompt help whenever needed.

A big thank you goes to Dr. Eskil Varenius, Dr. Gabriele Surcis and Dr. Anita Richards for supporting me during the hard times of data reduction and analysis, for the willing help and punctual response to my emails and for the valuable feedback. A great thank you to Dr. Magnus Persson who always provided insightful comments and suggestions. Many thanks also to all my work team for all the interesting scientific discussion and for teaching me more about the awesome life of stars.

A unique thanks to my dear friend and office mate Maryam, for making every working day nicer and nicer, and for all the funny times we spent together.

A further thanks to all my PhD fellows, the people at Onsala Space Observatory and at the Department of Space, Earth and Environment: it has been great to spend these years with you, sharing knowledge, ideas, experiences and culture.

Finally, one of my favourite authors, Neil Gaiman, once said: "Fairy tales are more than true: not because they tell us that dragons exist, but because they tell us that dragons can be beaten." Well, I would not have been here and I would not have tamed my dragon without the help, the encouragement and the love of my amazing family, my friends and Piero. Sometimes, just a postcard or a mail can make the difference between light and darkness. Last but not least, a sincere thanks to all the people at the U.O. Ematologia–Ospedale di Ravenna for all the kindness and the inestimable help you gave us.

Daria

Onsala, July 2017